molecular pharmaceutics

Article

Cite This: Mol. Pharmaceutics 2019, 16, 2430−2444

pubs.acs.org/molecularpharmaceutics

Tumor Targeting by Peptide-Decorated Gold Nanoparticles

Barbara Albertini,[†] Véronique Mathieu,[‡] Nunzio Iraci,[§] Matthias Van Woensel,[∥,⊥] Aurélie Schoubben,[†] Anna Donnadio,[†] Silvio M.L. Greco,[#] Maurizio Ricci,[†] Andrea Temperini,[†] Paolo Blasi,*[,¶] and Nathalie Wauthoz[⊥]

[†]Department of Pharmaceutical Sciences, University of Perugia, Via del Liceo, 1, 06123 Perugia, Italy

[‡]Laboratory of Experimental Cancerology and Toxicology, Faculty of Pharmacy, and [⊥]Laboratory of Pharmaceutics and Biopharmaceutics, Faculty of Pharmacy, ULB, Bvd du Triomphe CP207, 1050 Brussels, Belgium

[§]Department of Pharmacy, University of Salerno, Via Giovanni Paolo II, 132, 84084 Fisciano, Italy

[∥]Research Group Experimental Neurosurgery and Neuroanatomy, Laboratory of Pediatric Immunology, KU Leuven, 3000 Leuven, Belgium

[#]CNR-IOM—Istituto Officina dei Materiali, Strada Statale 14 km 163,5, 34149 Trieste, Italy

[¶]School of Pharmacy, University of Camerino, via Gentile III da Varano, 62032 Camerino, Italy

Supporting Information

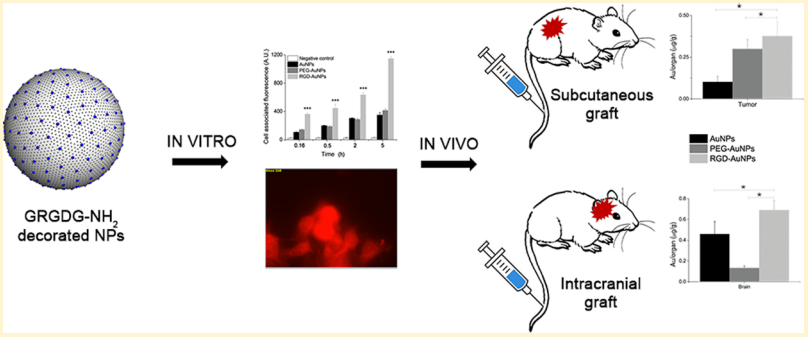

ABSTRACT: Cancer remains one of the most important challenges in biomedical sciences. Chemotherapeutic agents are very potent molecules that exhibit a significant level of toxicity in numerous tissues of the body, particularly in those characterized by high proliferative activity, such as the bone marrow. The scenario is even more complex in the case of the central nervous system, and in particular brain tumors, where the blood brain barrier limits the efficacy of drug therapies. Integrins, transmembrane proteins widely expressed in different types of cancer (glioblastoma, melanoma, and breast cancer), regulate the angiogenic process and play a pivotal role in tumor growth and invasion. Here, we report a nanotechnology strategy based on the use of AuNPs decorated with an arginine−glycine−aspartic acid-like peptide for the diagnosis and treatment of cancer. Two hours after administration in mice, the accumulation of the peptide-decorated NPs in the subcutaneous tumor was ∼4-fold higher than that of uncoated particles and ∼1.4-fold higher than that of PEGylated particles. Also, in the case of the intracranial tumor model, interesting results were obtained. Indeed, 2 h after administration, the amount of peptide-decorated particles in the brain was 1.5-fold that of undecorated particles and 5-fold that of PEGylated particles. In conclusion, this preliminary study demonstrates the high potential of this carrier developed for diagnostic and therapeutic applications.

KEYWORDS: *RGD-like peptide, αvβ3 integrin, melanoma, glioblastoma, nanomedicine*

INTRODUCTION

Cancer is one of the leading causes of death worldwide, accounting for 8.8 million deaths in 2015.[1] Even though promising results have been obtained over the past decades, it remains one of the most difficult challenges in biomedical science. Two significant limitations of traditional chemotherapy are its grave side effects and the ability of cancerous cells to develop drug resistance.[2] Indeed, drugs used in chemotherapy are very potent and exhibit significant toxicity in numerous tissues of the body, particularly in those characterized by high proliferative activity, such as the bone marrow.[3] Given their low selectivity, these drugs are administered at high doses, resulting in toxic effects that often make it necessary to decrease the dose or stop the therapy.[4] The scenario is even worst in the case of central nervous system cancers, especially brain tumors, because the blood brain barrier (BBB), which ensures brain homeostasis

Received: January 11, 2019
Revised: April 8, 2019
Accepted: April 10, 2019
Published: April 10, 2019

DOI: 10.1021/acs.molpharmaceut.9b00047
Mol. Pharmaceutics 2019, 16, 2430−2444

Scheme 1. Solution-Phase Synthesis of Pentapeptide Fmoc-Gly-Arg(Pbf)-Gly-fAsp(O*t*Bu)-Gly-NH_2 4a[a]

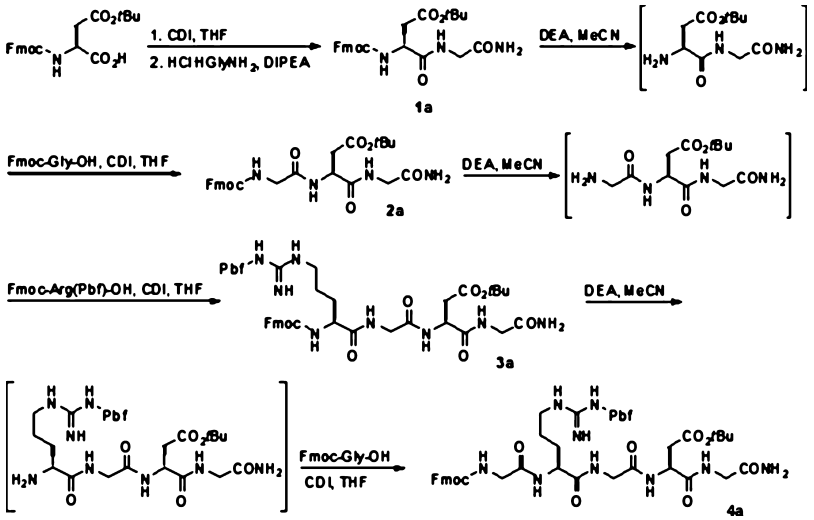

[a]DEA= diethylamine; Pbf= 2,2,4,6,7-pentamethyldihydrobenzo-furan-5-sulfonyl.

and restricts the passage of xenobiotics into the brain parenchyma, limits the access of anticancer drugs.[5] During the last two decades, researchers have developed new cancer treatments to overcome these challenges. Research has been focused on the discovery of novel molecular targets and the development of new chemotherapeutic agents and drug-delivery systems that are able to improve the accumulation of anticancer drugs at the tumor site.

Targeting the tumor vasculature is a good strategy that allows treatment of a wide range of tumors.[6] Because many different molecules are involved in angiogenesis, there are many potential targets for cancer treatment. According to Professor Judah Folkman, to obtain a more selective and effective cancer therapy, it is very important to target both cancer and endothelial cells.[7]

Integrins are transmembrane proteins characterized by 18 α subunits and 8 β subunits that give rise to 24 different receptors. Each subunit is characterized by three domains: a large extracellular domain involved in extracellular matrix protein binding, a single transmembrane domain, and a small cytoplasmic domain.[8] Integrins have no intrinsic enzymatic activity but activate after binding to extracellular ligands, clustering on the cell surface and undergoing conformational changes, which propagate across the membrane to the activated cytoplasmic kinase and cytoskeletal signaling cascades.[8,9]

Integrin signaling regulates diverse functions in tumor cells, including migration, invasion, proliferation, and survival.[10] Indeed, they are overexpressed in cells of invasive tumors, such as malignant glioma, melanoma, and breast cancer. Integrins also regulate the angiogenic process, playing a pivotal role in tumor growth and invasion. $\alpha v\beta 3$ integrins recognize the tripeptide sequence arginine−glycine−aspartic acid (RGD) present in many extracellular matrix proteins, such as fibronectin.[11]

In recent years, great progress has been made toward targeting integrins in cancer. Different integrin antagonists have proven to be effective in preclinical and clinical studies, and several peptidomimetic compounds, capable of blocking cell adhesion mediated by RGD, have been synthesized and tested.[12] One example is the conjugation of doxorubicin with an RGD-like peptide (Doxo-RGD), a formulation that has the same effect of free doxorubicin in vitro but showed greater tumor growth inhibition and a decrease in the size of metastases in mice in vivo. Doxo-RGD also appeared to be less toxic for the liver and heart than free doxorubicin.[13]

In this work, we report a nanotechnology approach based on the use of gold nanoparticles (AuNPs) decorated with an RGD-like pentapeptide for the diagnosis and treatment of cancer. This targeting moiety was selected for particle decoration because of its ability to recognize the $\alpha v\beta 3$ integrin.

EXPERIMENTAL SECTION

Materials. *O*-[2-(3-Mercaptopropionylamino)ethyl]-*O*-methylpolyethylene glycol (MeO-PEG-SH) ($M_w \approx 2000$ Da) was obtained from Sigma-Aldrich (Milan, Italy). Sodium azide, 3-(4,5-dimethylthiazol-2-yl)-2,5-diphenyltetrazolium bromide (MTT) and albumin were bought from Sigma-Aldrich (Brussels, Belgium). Rhodamine B polyethylene glycol thiol (RB-PEG-SH) was purchased from Nanocs Tebu-bio (Boechout, Belgium). Phosphate-buffered saline (PBS), ethylene diamine tetra acetic acid (EDTA), trypsin EDTA, glutamine, penicillin, streptomycin, gentamicin, fetal bovine serum (FBS), Roswell Park Memorial Institute (RPMI) medium, minimum essential medium (MEM), and Alexa fluor 488 goat anti-rabbit IgG (500 μL at 2 μg/μL) were obtained from Life Technologies (Merelbeke, Belgium), whereas formaldehyde was purchased from VWR (Leuven, Belgium). Rabbit anti-mouse $\alpha v\beta 3$ polyclonal antibody (100 μL at 1 μg/μL) was bought from Bioss (Huissen, The Netherlands). Ketamine and pentobarbital were obtained from Ceva (Brussels, Belgium), whereas xylazine was purchased from Prodivet Pharmaceuticals (Eynatten, Belgium). Nitric acid (HNO_3) and hydrochloric acid (HCl) were purchased from J. T. Baker (Milan, Italy). Ultrapure water was obtained from Milli-Q system (Millipore, Brussels, Belgium).

Peptide Design and Optimization. GRGDG-NH_2 and GRGDS were sketched and then submitted to a conformational search procedure in an implicit water solvent. The obtained conformational sets were used for two tasks: (i) to estimate probabilities of each conformer from the potential energies, assuming a Boltzmann distribution, and (ii) as input

DOI: 10.1021/acs.molpharmaceut.9b00047
Mol. Pharmaceutics 2019, 16, 2430−2444

conformations for the docking studies that used the crystal structure of integrin $\alpha v\beta 3$ in complex with a cyclic RGD-like peptide (cRGD—PDB ID: 1L5G) as target structure. Docking poses of the two peptides were selected on the basis of their predicted $\Delta G_{binding}$. The top-ranking GRGDG-NH_2/$\alpha v\beta 3$ integrin complex was subjected to a 10 ns-long molecular dynamics simulation to analyze the ligand/protein interaction. Additional details on the peptide design are reported in the Supporting Information.

Peptide Synthesis. A linear approach was selected for the preparation of gram quantity of the required pentapeptide **4a** (Scheme 1) using the Fmoc/*t*Bu strategy together with preactivation of the carboxylic acid function as the acyl-imidazole derivative. Under these experimental conditions, the solution-phase chemical synthesis of pentapeptide **4a** occurred without detectable epimerization with a global yield of 18% starting from Fmoc-Asp(O*t*Bu-OH) and with a low production cost. The use of Fmoc-L-amino acid selenoester derivatives of aspartate and glycine, as described by Temperini et al.,[14] for the preparation of dipeptide **1a** and tripeptide **2a** improved the global yield up to 30%. Unfortunately, this method was not applicable to the labile Pbf side chain of arginine. Additional details on the synthetic strategy are reported in the Supporting Information.

Nanoparticle Synthesis and Characterization. AuNPs were prepared using the Turkevich method: 20 mL of an aqueous solution of $HAuCl_4$ (0.25 mM) was heated to the boiling point under magnetic stirring. Then, the heat source was removed, and 1 mL of an aqueous solution of sodium citrate (1% w/v) was added to $HAuCl_4$ solution to reduce Au^{3+} to Au^0.

Particle morphology was characterized through transmission electron microscopy (TEM). The samples for TEM analysis were prepared by dropping 10 μL of the AuNP suspension on the surface of a 200 mesh Formvar-coated copper grid (TAAB Laboratories Equipment Ltd., Aldermaston, England), and the external phase of the suspension was evaporated overnight. TEM photomicrographs were elaborated using two different software: ImageJ and MatLab. ImageJ is a Java-based open source software developed at the National Institutes of Health,[15] whereas MatLab is a numerical computing environment characterized by high programming language (the MatLab script employed can be found in the Supporting Information).[16] In the image analysis, the particle size was expressed as mean projected area diameter (DP). Dynamic light scattering (DLS) was used to characterize the AuNPs in terms of size (mean hydrodynamic diameter, MHD) and stability. A Nicomp 380 autocorrelator (PSS Inc., Santa Barbara, CA, USA) equipped with a Coherent Innova 70-3 (Laser Innovation, Moorpark, CA, USA) argon ion laser was used for DLS measurements. The analyses were performed in triplicate at 20 °C for 15 min. The particle size was expressed as MHD ± standard deviation.

Nanoparticle PEGylation. Before preparing PEG-AuNPs, preliminary studies were performed to determine the adequate amount of HS-PEG-OMe (average molecular weight of 2 kDa, molecular weight distribution ≤ 1.1, Sigma-Aldrich, Milan, Italy) that was able to saturate the AuNP surface. Increasing amounts of MeO-PEG-SH were incubated for 24 h at 25 °C with the AuNP suspension. The mixtures were then centrifuged at 8000*g* for 1 h at 25 °C and washed three times; the supernatants were analyzed to quantify the amount of PEG not bound on the particle surface using the Ellman assay.[17−19] The Ellman assay was carried out to quantify the sulfhydryl groups not bound to the AuNP surface because of the ability of 5,5′-dithio-bis-(2-nitrobenzoic acid) (Ellman's reagent), also known as DTNB, to oxidize the thiol group, producing a mixed disulfide and 2-nitro-5-thiobenzoic acid (TNB). The concentration of sulfhydryl groups (c) was calculated using the Beer−Lambert law ($c = A/b\varepsilon$), where ε, the molar extinction coefficient of TNB, is equal to 14.150 M^{-1} cm^{-1}.[20] Data obtained using this assay were expressed as the number of molecules of HS-PEG-OMe per nm^2 (PEG/nm^2).[21,22] To calculate the number of NPs/mL of suspension, the following equation was used

$$\text{Number of AuNPs} = \frac{\mu\text{g of Au}}{\rho \cdot V}$$

where the μg of Au was determined using the inductively coupled plasma optical emission spectroscopy (ICP-OES) analysis (Varian Liberty Series II, Agilent Technologies, Milan, Italy).[22] The 242.795 nm emission line of Au was selected for the analysis, and each sample was analyzed in triplicate. A calibration curve was prepared in the concentration range of 0.5−15 ppm. V is the volume of one nanoparticle (NP), calculated considering a spherical shape particle with a size corresponding to the DP, and ρ is the density of gold. To calculate PEG/nm^2, expressing the density of PEG on the surface, the following equation was used

$$\text{PEG/nm}^2 = \frac{\text{PEG on AuNP surface/number of AuNPs}}{\text{AuNP surface}}$$

where PEG on the AuNP surface is the total number of PEG molecules bound to the particle surface.

To determine the PEG chain conformation on the AuNP surface, R_F (Flory radius) was calculated using the following equation

$$R_F = a \cdot N^{3/5}$$

where a is the monomer size (0.35 nm) and N is the number of monomers (44 monomers in the case of 2 kDa PEG); d, the distance between the anchorage site of two adjacent PEG chains, was calculated using the following equation[19,23,24]

$$d = 2\sqrt{\frac{1}{(\text{PEG/nm}^2)\cdot\pi}}$$

NP Decoration with the Peptide Moiety. An amino group of Fmoc-Gly-Arg(Pbf)-Gly-Asp(O*t*Bu)-Gly-NH_2 (1 mmol) was deprotected using 5 mL of diethanolamine in 2 mL of CH_3CN. The reaction mixture was maintained under magnetic stirring for 4 h at room temperature. The course of the reaction was monitored by thin-layer chromatography (TLC) (CH_2Cl_2/MeOH 85/15 v/v). The solution was then evaporated under reduced pressure, and the residue was washed with petroleum ether to remove dibenzofulvene. Gly-Arg(Pbf)-Gly-Asp(O*t*Bu)-Gly-NH_2 pentapeptide (0.005 mmol) was bound to HS-PEG-COOH (0.01 mmol) (average molecular weight of 2.1 kDa, molecular weight distribution ≤ 1.2, Sigma-Aldrich, Milan, Italy) using OxymaPure (0.01 mmol) and 1-ethyl-3-(3-dimethylaminopropyl)carbodiimide (0.01 mmol) as a coupling agent.[25,26] The reaction mixture was stirred under an argon atmosphere overnight. The course of the reaction was monitored by TLC (CH_2Cl_2/MeOH 85/15 v/v). The reaction mixture was then dried under reduced pressure. The residue was reacted with 2 mL of a mixture made

DOI: 10.1021/acs.molpharmaceut.9b00047
Mol. Pharmaceutics 2019, 16, 2430−2444

of H_2O/trifluoroacetic acid (TFA)/triethylsilane (2.5/95/2.5 v/v/v) to eliminate the orthogonal protecting group (*t*Bu and Pbf) of Asp and Arg.[27] The residue obtained was washed with diethyl ether, dried under reduced pressure, and then incubated with 2 mL of AuNPs at 25 °C for 24 h, after which the suspension was incubated with 20 mg of HS-PEG-OMe to obtain stealth particles.

To demonstrate the peptide deprotection and the successful particle decoration, the AuNPs were incubated with protected and deprotected PEGylated GRGDG-NH_2 and then characterized by ultraviolet−visible (UV−vis) spectroscopy using an Agilent 8453 spectrophotometer (Agilent, Waldbronn, Germany). UV−vis analyses were performed using the AuNP suspension as a blank to allow the detection of the characteristic adsorption peaks of Pbf, in the case of the protected peptide-functionalizing AuNPs.

To confirm the functionalization of NPs, RGD-AuNPs were characterized by Fourier-transform infrared (FT-IR) spectroscopy using a Jasco model 410 spectrometer equipped with a diffuse reflectance accessory (Jasco Europe srl, Lecco, Italy). The suspension (2 mL) was centrifuged to eliminate the byproduct of the coupling reaction and PEG not bound to the particle surface. The pellet was washed three times with water and then resuspended in water (2 mL). The suspension obtained was frozen and then freeze-dried. The sample for FT-IR analysis was prepared by adding KBr to the freeze-dried suspension. FT-IR spectra were recorded for pentapeptide, freeze-dried PEG-AuNPs, and freeze-dried RGD-AuNPs.

To calculate the peptide grafting density (number of GRGDG-NH_2 molecules per nm^2, RGD/nm^2), the ninhydrin assay was employed. The RGD-AuNP suspension (5 mL) was incubated with 5 mL of 12 M HCl at 100 °C for 24 h to hydrolyze the peptide bond. The mixture was then evaporated under reduced pressure, and the residue was solubilized in 500 μL of water. The ninhydrin reagent was solubilized in EtOH (25 mg/mL), and 500 μL of the ninhydrin solution was added to 500 μL of the sample solution. The mixture was allowed to react at 80 °C for 1 h before reading the absorbance at 570 nm. The calibration curve was prepared using a mixture of Gly/Asp/Arg (3:1:1) in the concentration range of 0.6−5 μM of total amino acid (r^2 = 0.997).

Fluorescent NPs. Fluorescent NPs were prepared to perform the in vitro analyses. NP suspensions were prepared as described above but with the addition of RB-PEG-SH (1 mg/mL of NP suspension) before the incubation at 25 °C for 24 h. The evaluation of RB-PEG-SH bound on the particle surface was determined indirectly after centrifugation of suspension at 8000*g* and quantification of RB-PEG-SH present in the supernatant using UV−vis analysis at λ of 558 nm. Additional information on fluorescent NPs is reported in the Supporting Information.

Cell Lines and Culture. Murine melanoma B16F10 (ATCC CRL-6475), murine gliosarcoma 9L (ATCC CRL-2926), and human glioblastoma U87 (ATCC HTB-14) cell lines were obtained from the American Type Culture Collection (ATCC, Rockville, USA). B16F10 and 9L cell lines were cultured in RPMI medium supplemented with 10% (v/v) FBS, while U87 cells were cultured using MEM supplemented with 5% (v/v) FBS. All media were supplemented with 0.6 mg/mL glutamine, 200 IU/mL penicillin, 200 IU/mL streptomycin, and 0.1 mg/mL gentamicin. All cell lines were maintained in 25 cm^2 flasks containing 5 mL of medium and incubated at 37 °C and 5% CO_2. B16F10 and 9L cells were split every 3 days when they reached 80% confluency, whereas U87 cells were split every 6 days when they reached the same confluency. Before performing the in vitro analyses, the cells were examined for mycoplasma using the Plasmo test TM (invivGen, USA) to assure the absence of mycoplasma contamination.

Evaluation of $\alpha v\beta 3$ Integrin Expression in B16F10, U87, and 9L Cell Lines. Cells (1×10^6) were detached using EDTA (10 mM in PBS) and fixed in 2% formaldehyde PBS solution for 30 min at room temperature and centrifuged at 200*g* (5 min). The supernatant was discarded, and the pellet was suspended in 1 mL of wash buffer (PBS containing 5% FBS and 0.1% sodium azide).[28] After 30 min of incubation at 37 °C and 5% CO_2, 100 μL of the anti-$\alpha v\beta 3$ integrin antibody (1:40 dilution in wash buffer) was added to the cell suspension, whereas 100 μL of the wash buffer was added to the negative control. The cell suspensions were then incubated at room temperature for 1 h and centrifuged; the supernatant was discarded, and the pellet was washed two times with the wash buffer. Alexa fluor 488 secondary antibody (100 μL; 1:400 dilution) was added, and the cells were incubated for 45 min at 37 °C and 5% CO_2. After the incubation, the samples were centrifuged, and the pellets were washed three times with PBS and suspended in 600 μL of PBS before performing the flow cytometry analyses using a Beckman Coulter FACS (Cell Lab Quanta) cytometer. To evaluate the integrin expression, the fluorescence levels were compared to three different controls: negative control, control containing the primary antibody alone, and control incubated with the fluorescent secondary antibody alone. Each formulation and control was analyzed in duplicate.

In Vitro Evaluation of Antiproliferative Activity. This assay, based on the reduction of MTT (yellow) to purple formazan in the mitochondria of living cells, is performed to evaluate cell proliferation by calculating the half maximal inhibitory concentration (IC50), which is the concentration of the compound that decreases the number of living cells by 50% after exposure to the compound. The number of living cells was determined after 72 h of culture in the presence of different formulations. The cells (5000 B16F10 cells/mL, 50 000 9L cells/mL and 25 000 U87 cells/mL) were seeded in a 96 well-plate (100 μL/well) and incubated at 37 °C and 5% CO_2 for 24 h before adding the following treatments at different concentrations: AuNPs, PEG-AuNPs, RGD-AuNPs (fluorescent and nonfluorescent), MeO-PEG-SH, and GRGDG-NH_2. NPs were employed in a concentration range between 0.1 and 50 μg/mL of gold;[29] MeO-PEG-SH was employed in a range of 0.0086 and 4.3 mg/mL, whereas GRGDG-NH_2 was tested in a concentration range between 1.08 and 540 μg/mL, the same concentrations contained in the NP suspension. After 72 h of incubation at 37 °C and 5% CO_2, the medium was replaced by the MTT solution (0.5 mg/mL, in medium without phenol red) for an additional 3 h. Then, the plates were centrifuged, the supernatants were discarded, and dimethyl sulfoxide (100 μL/well) was added to the well plates to dissolve formazan crystals for the absorbance measurement at 570 nm (with a reference of 630 nm). The experiments were performed in replicates of six.

Evaluation and Quantification of AuNP Uptake in B16F10. *Flow Cytometry Analyses.* B16F10 cells (1×10^6 cells/mL) were seeded in a 6-well plate (2 mL/well) and incubated for 24 h at 37 °C and 5% CO_2 before adding the fluorescent and nonfluorescent AuNP formulations (25 μg/mL

DOI: 10.1021/acs.molpharmaceut.9b00047
Mol. Pharmaceutics 2019, 16, 2430−2444

of gold). After 10 min, 30 min, 2 h, and 8 h of incubation, the cells were detached using trypsin−EDTA, centrifuged at 200*g* (5 min), washed three times with PBS, and suspended in 400 μL of PBS for flow cytometry analysis with Cell Lab Quanta. The assay was performed in triplicate.

Competition Assay. Cells (1×10^6 B16F10 cells/mL) were seeded in a 6-well plate (2 mL/well) and incubated for 24 h at 37 °C and 5% CO_2. The medium was removed, and then the cells were preincubated for 25 min with the anti-$\alpha v\beta 3$ integrin antibody (diluted 1:40 in FBS free medium) and washed three times with PBS before adding the three fluorescent AuNP formulations at a concentration of 25 μg/mL of gold for 2 h. Next, the cells were detached using trypsin−EDTA, and the pellets were washed three times using PBS and suspended in 400 μL of PBS for the flow cytometry analyses.[30] The assay was performed in triplicate.

Fluorescent Microscopy. Coverslips were transferred into six individual wells of a 6-well plate before adding the B16F10 cells. Cells were then seeded in a 6-well plate and incubated for 24 h at 37 °C and 5% CO_2. The fluorescent NP formulations containing 25 μg/mL of gold were added. After 10 min, 30 min, 2 h, and 8 h of incubation, the cells were washed using PBS, and the coverslips were placed over the glass slides before performing the fluorescence microscopy analyses (fluorescence microscope, Zeiss) using the following parameters: fluorescent channel: red (Alexa 494); exposure time: 48 ms; magnification: 40×. Three images per condition were taken. The assay was performed in duplicate.

TEM. B16F10 cells were seeded in a 6-well plate and incubated for 24 h at 37 °C and 5% CO_2 before adding the NP formulations containing 25 μg/mL of gold. After 2 h of incubation, the medium was discarded, and the cells were detached using trypsin (and then neutralized using complete medium), centrifuged at 200*g* (5 min), washed using PBS, and fixed in formaldehyde (4% w/v in PBS) and glutaraldehyde (1% w/v in PBS). The cells were then centrifuged, the supernatant was discarded, and the pellets were dehydrated using EtOH and treated with propylene oxide. Cells were embedded in Epon-Araldite resin, and resin slices were obtained using Microtome (Reichert-Jung Ultracut E microtome, Leica Microsystem Spa, Milan, Italy) before performing TEM (Philips EM 400T microscope, Eindhoven, Holland) analyses.[31]

B16F10 Network Assay. *Inhibition of B16F10 Network Formation.* Matrigel (BD Pharmingen) (150 μL/well) was put into a 24-well plate and incubated at 37 °C and 5% CO_2 to promote the gel formation. B16F10 cells (1×10^5 cells/well) were then seeded in the presence or absence of formulations (or the anti-$\alpha v\beta 3$ integrin antibody). Five pictures per well (three wells per experimental condition) were taken at different time points (16, 24, and 48 h) to investigate the network formation.[32] NP suspensions, all compounds, and their relative concentrations are reported below:

AuNPs ([Au] = 40 μg/mL); PEG-AuNPs ([Au] = 50 μg/mL); RGD-AuNPs ([Au] = 20 μg/mL); RGD-AuNPs ([Au] = 10 μg/mL); GRGDG ([GRGDG-NH_2] = 340 μg/mL); GRGDG ([GRGDG-NH_2] = 108 μg/mL); anti-$\alpha v\beta 3$ antibody was added using a dilution of 1:100. The experiment was performed in triplicate.

B16F10 Network Disruption. For the analysis of the network disruption, similar procedures were conducted, but the cells were seeded in the absence of treatment for 8 h to allow the formation of the network. Then, fresh medium containing NP suspensions or control solutions was added to the B16F10 network and incubated for another 24 h. Pictures were taken at different time points (t = 0, 2, 4, 8, and 24 h). NP formulations and control substances were used at the same concentrations reported above. The experiment was performed in triplicate.

Biodistribution in Tumor-Based Grafted B16F10 Cells. *Experimental Animals.* B6D2F1 mice (18−22 g, Charles Rivers, Arbresle, France) aged 4−6 weeks were used for the in vivo experiments. The mice were maintained at 22 ± 2 °C and 55 ± 10% of relative humidity. They were subjected to a 12 h/12 h light and darkness cycle and received food (Carfil, Oud-Turnhout, Belgium) and water ad libitum. All animal experiments were approved by the institutional ethics committee (CEBEA-Commission d'Ethique du Bien-Être Animal, Université Libre de Bruxelles). The laboratory federal agreement number is LA1230568.

Subcutaneous Graft. B16F10 cells (2.5×10^5) were suspended in 200 μL of a mixture of Matrigel/FBS-free RPMI (20:80, v/v) and inoculated subcutaneously in the left flank of mice, previously anesthetized by intraperitoneal injection of ketamine (112.5 mg/kg) and xylazine (1.5 mg/kg).[33] When the tumor reached a surface area of 150−200 mm^2, 200 μL of suspensions containing AuNPs, PEG-AuNPs, and RGD-AuNPs (gold concentration, 50 μg/mL) were administered through the tail vein. The mice (four mice/time) were then sacrificed, using a lethal injection of pentobarbital, 2 and 8 h after particle administration. The blood was withdrawn by cardiac puncture, collected in heparinized tubes, and centrifuged at 3000*g* for 15 min at 4 °C to obtain the plasma. Plasma was stored at −80 °C before performing the gold quantification. Tumor, brain, kidney, lung, liver, heart, and spleen were surgically removed and stored at −80 °C until gold quantification.

Intracranial Graft. B16F10 cells (1×10^5) were suspended in 50 μL of FBS-free RPMI medium and inoculated in the brain parietal region of mice, previously anesthetized by intraperitoneal injection of ketamine (112.5 mg/kg) and xylazine (1.5 mg/kg). Five days after tumor injection, 200 μL of suspensions containing AuNPs, PEG-AuNPs, or RGD-AuNPs (gold concentration, 50 μg/mL) were administered through the tail vein. The mice were sacrificed at the same time points (five mice/time), following the same procedure reported for subcutaneous graft. The plasma and organs were collected and stored as in the previous sections.

Gold Extraction and Quantification. Tumor and organs were weighted precisely and digested in 2 mL of aqua regia (HCl/HNO_3, 1/3 v/v). The mixture was sonicated for 1 h at room temperature, and then aqua regia was added to reach a final volume of 4 mL. Plasma was treated in the same way.[34] The solutions obtained were degassed overnight at room temperature to remove chlorine gas and nitric oxide before performing the ICP-OES analysis (Varian Liberty Series II, Agilent Technologies, Milan, Italy). The ICP-OES analyses were performed under the same experimental conditions described above.

Statistical Analysis. Comparison of results from in vitro analyses was carried out by one-way analysis of variance (ANOVA), while in vivo results were evaluated using the Kruskal−Wallis test because the Cochran's c test was significant. All data were provided as mean plus or minus standard deviation, and a p-value < 0.05 was considered significant.

DOI: 10.1021/acs.molpharmaceut.9b00047
Mol. Pharmaceutics 2019, 16, 2430−2444

RESULTS

Molecular Modeling Studies. Integrins are particularly interesting molecular targets exploited in cancer therapy because of their overexpression in many tumors and their involvement in the angiogenic process, which plays a pivotal role in tumor growth and invasion.[35−39] $\alpha v\beta 3$ integrin has been previously targeted by RGD-grafted PLGA-NPs loaded with paclitaxel.[40] Considering the interesting data collected by Danhier et al. (2009) and following the suggestions from molecular modeling studies, we designed the GRGDG-NH_2 pentapeptide to decorate AuNP for cancer theranostic applications.

Using the crystal structure of $\alpha v\beta 3$ integrin in complex with the cRGD,[35] we built an in silico model of the integrin in complex with GRGDS employed in previous studies,[40] and we estimated the $\Delta\Delta G_{binding}$ of compounds GRGDS and cRGD (Table 1).

Table 1. Prime-Predicted $\Delta\Delta G$ Values of $\alpha v\beta 3$ Integrin Binding to the Different RGD-like Peptide

ligand	$\Delta\Delta G^a$	ligand strain[b]
cRGD	0	4.48
GRGDS	+5.05	11.05
GRGDG-NH_2	+3.69	4.09

[a]Prime-predicted $\Delta\Delta G_{binding}$ (kcal/mol). [b]Prime-predicted ligand strain (kcal/mol).

It is worth noting that GRGDS showed a very high ligand strain energy compared to cRGD, suggesting a suboptimal interaction with the target integrin. Intrigued by the high ligand strain of GRGDS, we investigated its conformational behavior in solution, and we found that the influence of the serine residue side chain could strongly stabilize the biologically inactive tangled conformation. The global minimum conformation of GRGDS (Figure 1A), whose conformer probability in water was estimated to be higher than 0.8, shows a network of polar interactions involving the serine hydroxyl group and its terminal carboxyl, the terminal amino group of the glycine residue, the backbone NHs of the arginine and aspartate residues, the arginine guanidine group, and the sidechain carboxyl of the aspartate residue.

Aiming at the minimization of the conformational energy gap between the bioactive and this energy minimum conformation, we thought to weaken these interactions through removal of the serine side chain and amination of the terminal carboxyl group to give GRGDG-NH_2. This idea was even endorsed by a potential gain in the exopeptidase resistance through the amination of the terminal carboxyl.

GRGDG-NH_2 was submitted to the same calculations we ran for the GRGDS, and an improvement of the predicted $\Delta G_{binding}$ as well as a decrease in the ligand strain energy, compared to GRGDS, were observed (Table 1). GRGDG-NH_2 docks similarly to GRGDS and to the experimental bound conformation of cRGD (Figure 1B).

Most of the peptide−protein interactions take place at the arginine and aspartate side chains. Indeed, during a 10 ns-long molecular dynamics (MD) simulation, the arginine group directly interacts with Gln180 and Asp150 and with Asp218, Tyr178, and Ala213 through the mediation of water molecules. The carboxylate group strongly interacts with the Mn ion bound at the metal ion-dependent adhesion site (MIDAS) and with Asn215 and Tyr122 (Figure 1C).

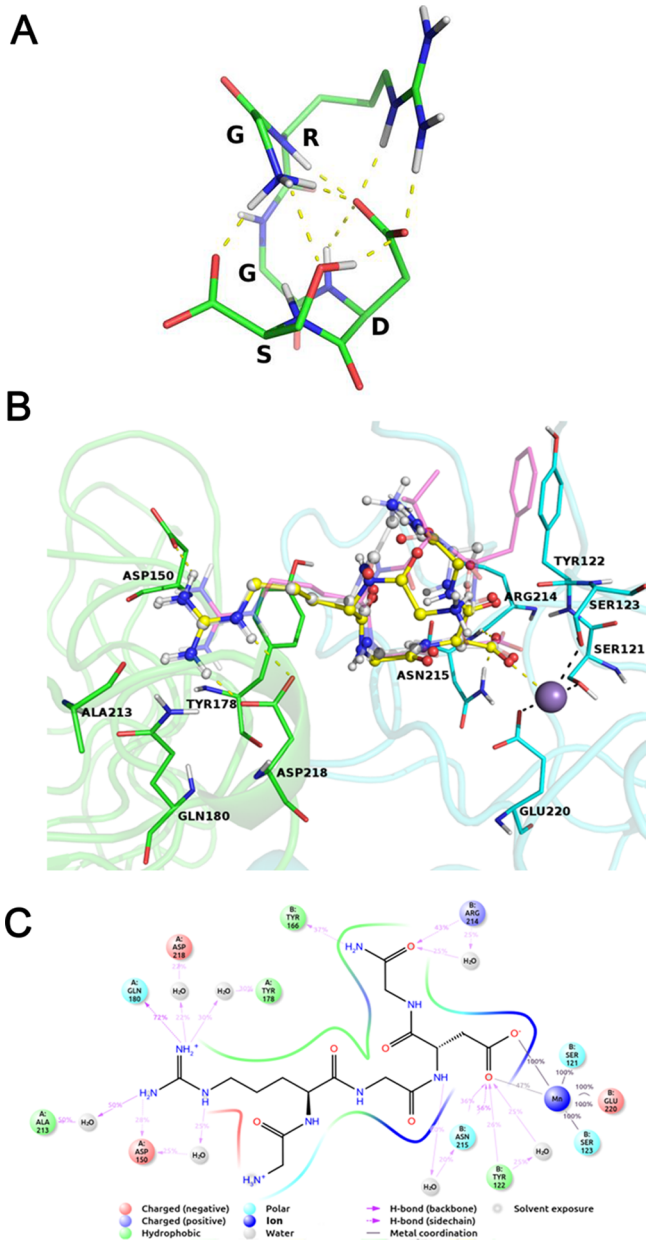

Figure 1. (A) Global minimum conformation of GRGDS, depicted in sticks. Intramolecular polar interactions are shown as yellow dashed lines. (B) Best docked models of GRGDG-NH_2 (yellow sticks and balls) and GRGDS (white balls and sticks). Integrin residues are depicted in green cartoons and sticks (αv subunit) and in cyan cartoons and sticks ($\beta 3$ subunit). cRGD bound conformation is shown in transparent magenta sticks for reference. Coordination and hydrogen bonds are shown in black and yellow dashes, respectively. Manganese ion bound at the MIDAS is depicted as a purple sphere. (C) Integrin $\alpha v\beta 3$/GRGDG-NH_2 interaction diagram reporting interactions with more than 0.2 occupancy during a 10 ns long MD trajectory.

Peptide Synthesis. The dipeptide Fmoc-Asp(O*t*Bu)-Gly-NH_2, the starting point of the pentapeptide synthesis, was synthesized by different procedures, and method D, the most convenient one in terms of yield and purity, was chosen as a base for the successive steps (Supporting Information).

DOI: 10.1021/acs.molpharmaceut.9b00047
Mol. Pharmaceutics 2019, 16, 2430−2444

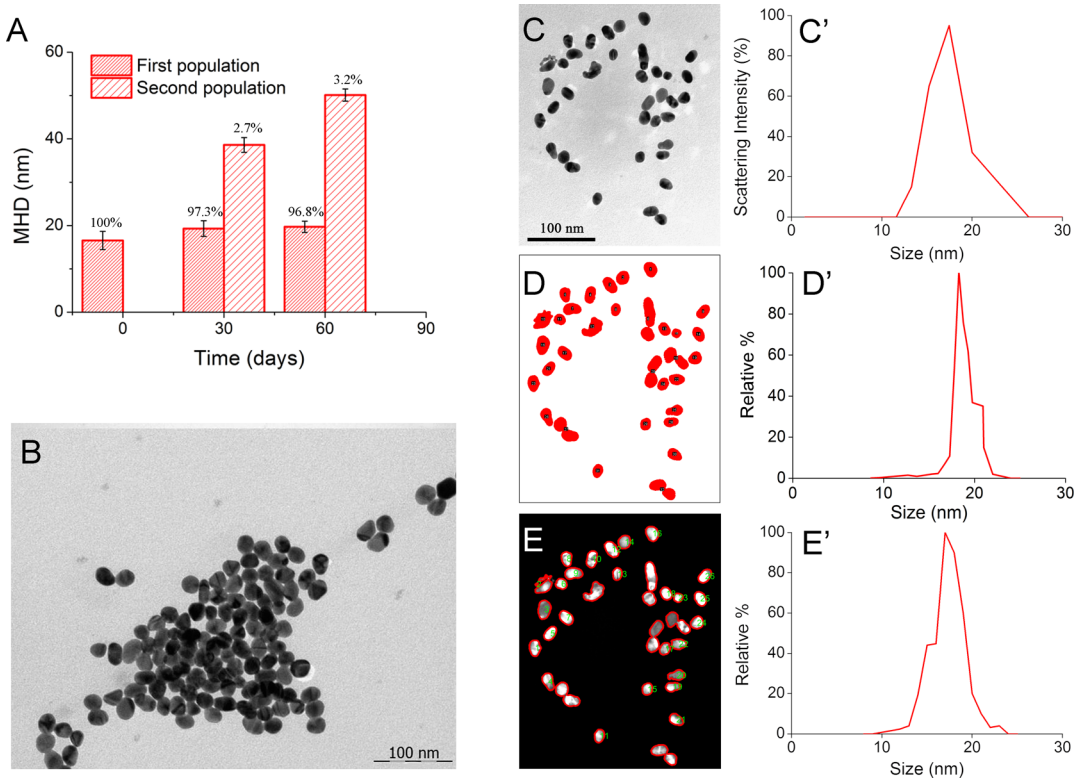

Figure 2. (A) Particle size immediately after preparation and over time; (B) TEM sample photograph of AuNPs; (C) TEM photograph of AuNPs and (C′) particle size distribution obtained by DLS; (D) photograph elaborated using ImageJ and (D′) relative particle distribution; (E) photograph elaboration using MatLab and (E′) relative particle size distribution.

The detailed total synthesis of the pentapeptide is reported in Scheme 1. This synthesis was performed in liquid phase using the Fmoc/*t*Bu strategy. Fmoc was selected as the *α*-amino protecting group because it is cleaved under mild basic conditions and is stable under the acidic conditions needed for side chain deprotection when using *t*Bu and Pbf for aspartic acid and arginine protection, respectively.

The possible arginine and/or aspartic acid racemization was monitored by ^{13}C nuclear magnetic resonance (NMR), which allowed investigation of the presence of diasteroisomers with a sensitivity of 2%. ^{13}C NMR spectra did not reveal the presence of diasteroisomers in tetrapeptide **3a** and pentapeptide **4a** (Scheme 1, Supporting Information).

High-performance liquid chromatography−high resolution mass spectrometry had confirmed the purity of the protected pentapeptide: the peak with a retention time of 6.591 min was characterized by an exact mass of 990.43951 $[M + H]^+$ Da. The calculated mass for $C_{48}H_{63}N_9O_{12}S$ is 989.43964 Da (Supporting Information).

The liquid-phase synthesis made it possible to obtain the final product in ∼18% global yield starting from Fmoc-Asp(O*t*Bu)-OH with a low production cost. To increase the yield of the total synthesis, dipeptide **1a** and tripeptide **2a** (Scheme 1) were also synthesized in ∼94 and ∼89% yields, respectively, using the Fmoc-L-amino acid selenoesters derivatives as described by Temperini et al. (Supporting Information).[14] It was not possible to use the same strategy for the tetrapeptide and pentapeptide syntheses because of the lability of the Pbf arginine protecting group in the presence of benzenselenol.

AuNP Synthesis and Characterization. The Turkevich method allowed the preparation of NPs characterized by an MHD of 16 ± 2 nm (Figure 2A) that appeared not perfectly spherical under the electron microscopy observation (Figure 2B). Particles mean DP, determined from TEM images using ImageJ or MatLab, were 15 ± 3 and 16 ± 2 nm, respectively (Figure 2D′,E′). Particle DP, determined from TEM images, was slightly different from DLS measurements because DLS estimates NP MHD, that is, the diameter of an equivalent rigid sphere considering its hydration layer,[41] whereas image analysis estimates DP, defined as the diameter of a circle having the same area of one particle without considering the hydration layer.[42]

As expected, the presence of PEG on AuNPs produced a shift of the MHD from 16 to 35 nm, in accordance with the report of Li and co-workers, which showed a growth of PEGylated NP size with the increase of the grafting density.[43] In addition, RGD-AuNPs were characterized by an MHD around 37 nm (37.1 ± 2.5 nm), not significantly different from that of PEG-AuNPs (Figure 3A).

The ninhydrin assay allowed evaluation of peptide density (number of GRGDG-NH_2 molecules per nm^2, RGD/nm^2) on the NP surface, obtaining a value of 0.64 RGD/nm^2 (Supporting Information). From this data, a PEG/ligand density ratio of 21.11 was calculated, and a simulation of the comparative size of the bare AuNP, of the PEG coating, and of the RGD functionalization layer is displayed in Figure 3B.

For better visualization, the model particle has been pictured with the single PEG chains (small gray dots) and the RGD molecules (large blue dots) exposed on the particle surface, assuming a homogeneous distribution on the particle surface (Figure 3C).

Evaluation of *αvβ*3 Integrin Expression in B16F10, U87, and 9L Cell Lines. The expression of *αvβ*3 integrin in

DOI: 10.1021/acs.molpharmaceut.9b00047
Mol. Pharmaceutics 2019, 16, 2430−2444

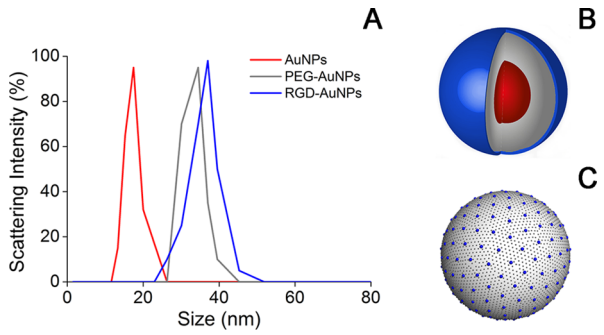

Figure 3. (A) Particle size distribution determined by DLS of AuNPs, PEG-AuNPs, and RGD-AuNPs; (B) simulation of the comparative size of RGD-AuNPs where the inner red core is the bare AuNP, the gray layer is the PEG coating, and the outer blue layer is the RGD functionalization; (C) AuNP surface where PEG chains correspond to the small gray dots and RGD peptides to the larger blue dots.

three different cancer cell lines (U87, B16F10, and 9L) was evaluated by flow cytometry. B16F10 and U87 expressed high levels of $\alpha v\beta 3$ integrin protein, with 54 and 81% of positive stained cells, respectively.[44,45] On the contrary, 9L cells expressed much lower levels of $\alpha v\beta 3$ integrin (9% of positive stained cells) (Figure 4).

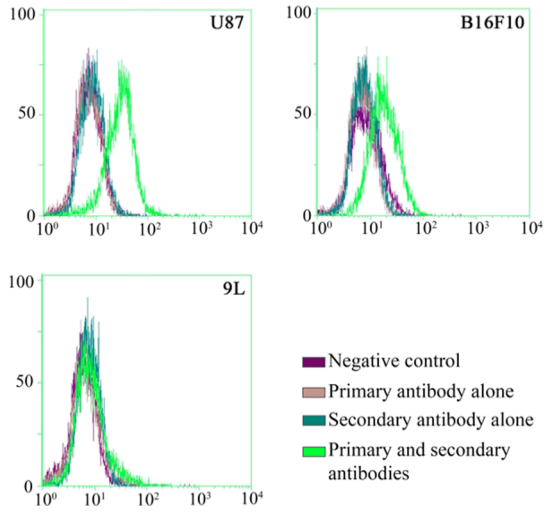

Figure 4. Fluorescence signals for the $\alpha v\beta 3$ integrin expression in B16F10, U87, and 9L cell lines.

In Vitro Antiproliferative Activity. The in vitro growth inhibitory activity of the different NP formulations was examined using the MTT colorimetric assay. The in vitro concentration of each compound that induced a 50% reduction of global cell growth (IC50) was identified (Table 2).[46] Fluorescent and nonfluorescent AuNPs and PEG-AuNPs showed similar IC50 values when incubated with the three different cell lines (Table 2), regardless of the differences in the $\alpha v\beta 3$ integrin expression.[47] On the contrary, fluorescent and nonfluorescent RGD-AuNPs were characterized by the lowest IC50 in U87 and B16F10, whereas these particles were 2-fold less active on the 9L cell line.

The complete set of data of cell viability versus concentration of the different formulations for U87, B16F10, and 9L cell lines are reported in the Supporting Information.

Table 2. IC50 Values of Different Formulations on Three Cell Lines

	IC50 ± S.D. (μg/mL)		
sample	B16F10	U87	9L
AuNPs	40 ± 1	40 ± 2	40 ± 1
RB-AuNPs	40 ± 2	40 ± 1	40 ± 3
PEG-AuNPs	45 ± 2	45 ± 2	>50
RB-PEG-AuNPs	>50	45 ± 3	>50
RGD-AuNPs	20 ± 1	20 ± 2	40 ± 2
RB-RGD-AuNPs	25 ± 3	20 ± 1	40 ± 3
GRGDG	340 ± 12	270 ± 8	432 ± 15
OMe-PEG-SH	>4300	>4300	>4300

NP Uptake Quantification and Mechanism. B16F10 was selected for further in vitro and in vivo characterizations even though U87 expressed high levels of $\alpha v\beta 3$ integrin protein because B16F10 animal models were considered more convenient (please see below).

The degree of NP cellular uptake and/or adsorption on B16F10 cells was quantified by flow cytometry using fluorescent AuNP formulations (Figure 5A). B16F10 cells were able to adsorb and/or internalize all tested formulations. The differences between AuNPs and PEG-AuNPs were not significant, whereas the fluorescent signal of cells treated with RGD-AuNPs was higher than those of cells treated with the other formulations ($p < 0.001$).

To ascertain whether the cell uptake of RGD-AuNPs is due to integrin binding, a competition assay was performed. When B16F10 cells were preincubated with anti-$\alpha v\beta 3$ antibodies, RGD-AuNP uptake was reduced, and the fluorescence signal became almost equivalent to that of AuNP- and PEG-AuNP-treated cells[30] (Figure 5B).

Images acquired by fluorescence microscopy confirmed the data obtained by flow cytometry. Indeed, for each formulation, with the increase in incubation time, there was an increase in the cellular uptake. As shown in Figure 6A, the RGD-AuNPs were more internalized by B16F10 than the other formulations at each time point, but after 8 h of incubation, the RGD-AuNP fluorescent signal was almost saturated.

Observing the fluorescent microscopy images, it seemed that the particles were internalized into the cells, but to gain reliable information on the NP location, TEM analyses were performed, as the high electron density of gold makes it easy to detect particles with this method. In fact, the TEM analysis demonstrated that the NPs in the three different formulations were internalized by the cells and not merely bound to the surface (Figure 6B).

Effect of NPs on B16F10 Network Formation and Disruption. When the B16F10 cell line is grown on Matrigel, a complex protein mixture able to simulate the extracellular matrix, it forms a characteristic network similarly to the way human umbilical vein endothelial cells do. By studying how compounds or NPs affect the network formation or disrupt it upon formation, we can obtain information about their ability to prevent or minimize the migration of cancerous cells and thus to limit tumor invasion and angiogenesis.[48]

The formation of a network comparable to the control (untreated B16F10) was observed when B16F10 cells were treated with AuNPs and PEG-AuNPs (Figure 7A). On the contrary, the anti-$\alpha v\beta 3$ integrin antibody (positive control), GRGDG-NH_2 pentapeptide, and RGD-AuNPs drastically

DOI: 10.1021/acs.molpharmaceut.9b00047
Mol. Pharmaceutics 2019, 16, 2430−2444

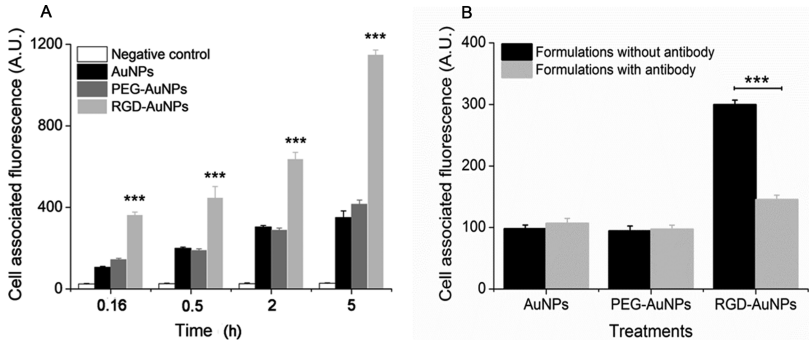

Figure 5. (A) Uptake of NPs by B16F10 cells investigated by flow cytometry analysis. Data are expressed as mean ± SD (n = 3); ***p < 0.001 by one-way ANOVA. (B) Competition assay performed on the B16F10 cell line. Data are expressed as mean ± SD (n = 3); ***p < 0.001 by one-way ANOVA.

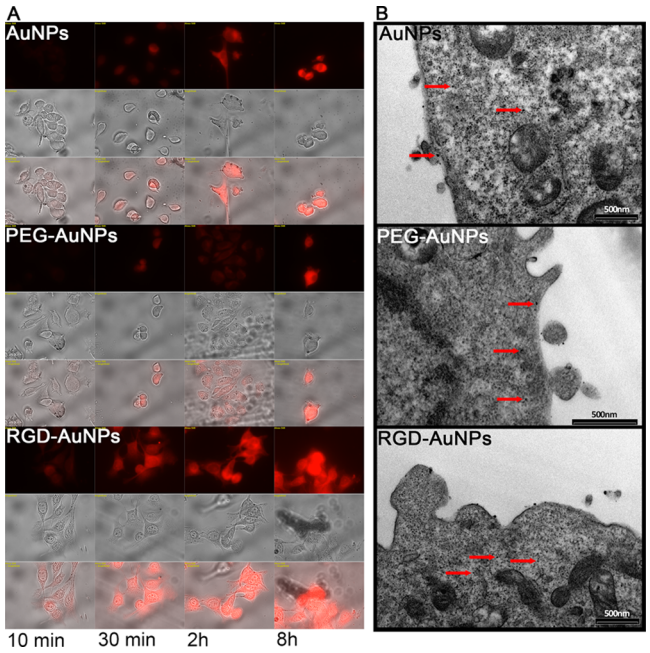

Figure 6. (A) Fluorescence microscopy images, exposure time 48 ms (first row of each panel), phase contrast microscopy images (second row of each panel), and merge (third row of each panel) of fluorescent AuNPs, PEG-AuNPs, and RGD-AuNPs at different time points. Magnification 40×. (B) Transmission electron photomicrographs of fluorescent AuNPs, PEG-AuNPs, and RGD-AuNPs internalized into B16F10 cells after 2 h of incubation. Red arrows indicate some of the NPs internalized.

decreased melanoma cell migration and inhibited the formation of the network (Figure 7A).

In a different experimental setup, where the network was let to form and the treatments added later on, it was possible to assess the ability to destroy an already formed network. In this specific case, AuNPs, PEG-AuNPs, and the anti-$\alpha v\beta 3$ integrin antibody were unable to damage B16F10 networks: at each time point, differences with the negative control were negligible. RGD-AuNPs and GRGDG-NH_2 at IC50 concentrations seemed able to destroy only the interconnecting channels, whereas RGD-AuNPs and GRGDG-NH_2 at a concentration lower than IC50 slowly destroyed the network, with complete disruption after 24 h of incubation (Figure 7B).

In Vivo Biodistribution and Tumor Targeting. Given the promising results obtained in vitro, GRGDG-NH_2-decorated AuNPs were tested in vivo in two different B16F10 tumor models, namely, subcutaneous and intracranial. As the theranostic application of GRGDG-NH_2-decorated AuNPs in brain tumors would be extremely interesting, the subcutaneous model was chosen for its reproducibility, easy localization of the tumor, and tendency to metastasize in the brain,[49] whereas the intracranial model was chosen to assess the targeting ability to brain tumors.

In the subcutaneous graft model (Figure 8), AuNPs were mainly detected in the liver and spleen, the main organs of the reticuloendothelial system (RES), whereas the accumulation in the tumor was negligible. Two hours after injection, AuNPs had completely disappeared from the plasma, and 8 h after administration, gold was detectable only in the liver and spleen, the main RES organs (Figure 8). This behavior can be attributed to the absence of PEG on the particle surfaces, allowing fast opsonization and removal from the bloodstream.

PEG-AuNPs were also detected in the spleen but they were characterized by a higher plasma half-life with still high amounts of gold in the plasma 8 h after administration. PEG-AuNPs reached the tumor site and accumulated in higher amounts than the bare AuNPs as a consequence of their long time in circulation and enhanced permeability and retention effect (Figure 8).[50−52]

Similar to PEG-AuNPs, RGD-AuNPs also showed a plasma half-life higher than that of AuNPs, but their accumulations in liver and spleen were significantly lower.

Their accumulation in the tumor was 1.2-fold higher than that of PEG-AuNPs (*p < 0.05) and 3.7-fold higher (*p < 0.05) than that of AuNPs. It is interesting to note that 2 hours after administration, RGD-AuNPs were detected in significantly higher amounts in the lungs and brain. After 8 h, RGD-AuNPs still persisted in the tumor site.

In the intracranial graft model (Figure 9), AuNPs accumulated prevalently in the liver and spleen, whereas they disappeared from the plasma 2 h after injection. As previously explained, this trend may be attributed to the absence of PEG on particle surfaces, which meant that opsonins were adsorbed on the surface of AuNPs, which were then removed from the bloodstream. Indeed, 8 h after AuNP administration, gold was present only in the liver and spleen (Figure 9). These NPs were also characterized by high accumulation levels in the heart 2 h after administration, whereas PEG-AuNPs and RGD-AuNPs did not exhibit the same trend (Figure 9).

PEG-AuNPs were characterized by higher levels of gold in the plasma because of the presence of PEG on particle surfaces. Also, 8 h after particle administration, high levels of gold were found in the liver and spleen. RGD-AuNPs showed low

DOI: 10.1021/acs.molpharmaceut.9b00047
Mol. Pharmaceutics 2019, 16, 2430−2444

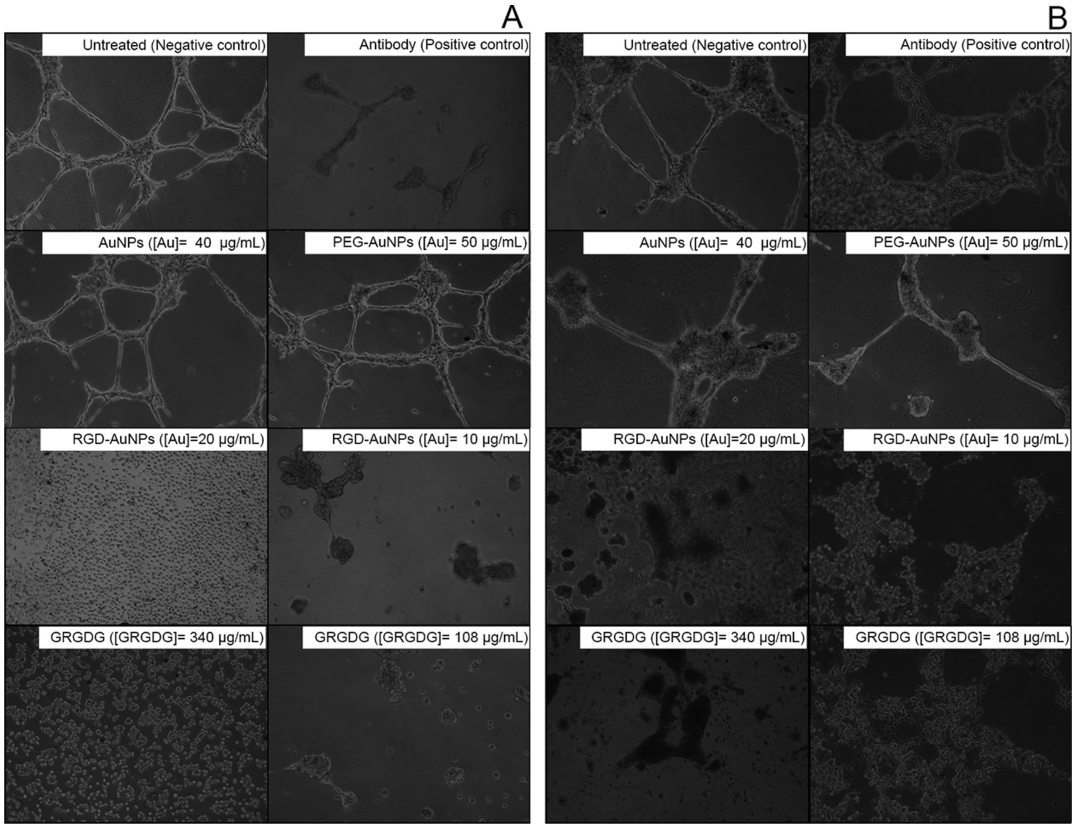

Figure 7. (A) B16F10 network formation inhibition assay of different formulations (time point = 16 h). (B) B16F10 network disruption assay of different formulations (time point = 24 h). Magnification 10×.

accumulation in the liver and spleen and showed accumulation in the brain ∼5-fold higher than that achieved by PEG-AuNPs ($*p < 0.05$) and 1.5-fold higher than that of AuNPs ($*p < 0.05$), 2 h after administration. After 8 h, RGD-AuNPs persisted in the brain, whereas the other two formulations were undetectable (Figure 9B).

DISCUSSION

Our data obtained by flow cytometry analyses are thus in agreement with previous reports.[53−55] The association of the $\alpha v\beta 3$ integrin expression with tumor neoangiogenesis has been studied extensively in aggressive highly malignant tumors,[56] and $\alpha v\beta 3$ integrins have been found overexpressed by a variety of tumors, such as melanoma, glioma, multiple myeloma, ovarian, renal, and breast cancers.[57] Interestingly, $\alpha v\beta 3$ integrins are also overexpressed in blood vessels in tumor sites.[58]

The RGD-AuNPs produced a substantial decrease of cell growth over 72 h in cell lines characterized by high levels of $\alpha v\beta 3$ integrin, whereas the IC50 and then the ability to decrease the cell growth in 9L did not change with the RGD surface modification (Table 2). For this reason, it can be speculated that RGD-AuNPs have the highest effect because of the presence of GRGDG-NH_2 on the particle surfaces.[59] The sole pentapeptide presented some antiproliferative effect on B16F10 and U87, probably due to the $\alpha v\beta 3$ integrin binding and signal transduction (Table 2).[60] The other component of NPs, MeO-PEG-SH, when tested alone, led to a higher IC50 than the highest concentration tested, demonstrating its low cytotoxicity.[61] Because no differences between fluorescent and nonfluorescent NPs were observed, it is possible to assert that RB-PEG-SH did not influence the interaction between integrins and the NP targeting moiety.

Since the main aim of the present work was to evaluate the ability of GRGDG−NH_2-decorated NPs to target tumor cells expressing $\alpha v\beta 3$ integrin, the B16F10 cell line was chosen for further studies. In fact, even if U87 showed a higher expression of $\alpha v\beta 3$ integrin, B16F10, which is a melanoma cell line, tends to metastasize to the brain, and the black color of the cell clusters/tumor mass due to melanin production makes it easy to identify the tumor.

It was expected that the presence of the polymer on the PEG-AuNP surface would cause lower uptake of these particles than of AuNPs because of the hydrophilic "cloud" that can hinder the interaction with the cell membrane.[62] Instead, we observed a similar uptake of PEG-AuNPs and AuNPs (Figure 5A). This can be explained by the high adsorption of albumin (present in the cell medium) on the AuNP surface.[63] Increased protein adsorption keeps the particles in suspension longer, and consequently, they are less in contact with cells.[64] Furthermore, albumin is negatively charged at a pH of 7.4, and this negative charge could hinder the interaction between particles and negatively charged cell membranes.[65] Results obtained by flow cytometry revealed that all particles were effectively adsorbed and/or internalized, but the uptake efficiency depended on the presence of GRGDG-NH_2 pentapeptide on the particle surface (Figure 5A). The improvement in the uptake of peptide-decorated NPs by the B16F10 cell line is in agreement with the cytotoxicity data obtained by the MTT assay. This strongly supports that adsorption/uptake is determined by $\alpha v\beta 3$ integrin binding mediated by the RGD sequence.[66,67] RGD-like peptides have

DOI: 10.1021/acs.molpharmaceut.9b00047
Mol. Pharmaceutics 2019, 16, 2430−2444

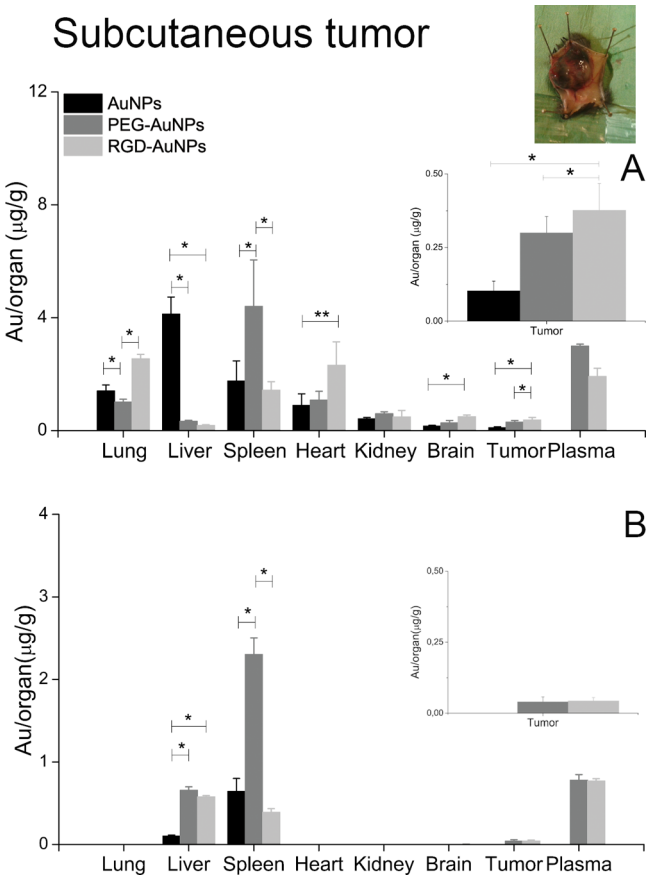

Figure 8. Quantitative biodistribution of intravenously injected NPs 2 h (A) and 8 h (B) after administration in mice grafted with the subcutaneous tumor. Data are expressed as mean ± SD; *p < 0.05, **p < 0.01 by Kruskal–Wallis test.

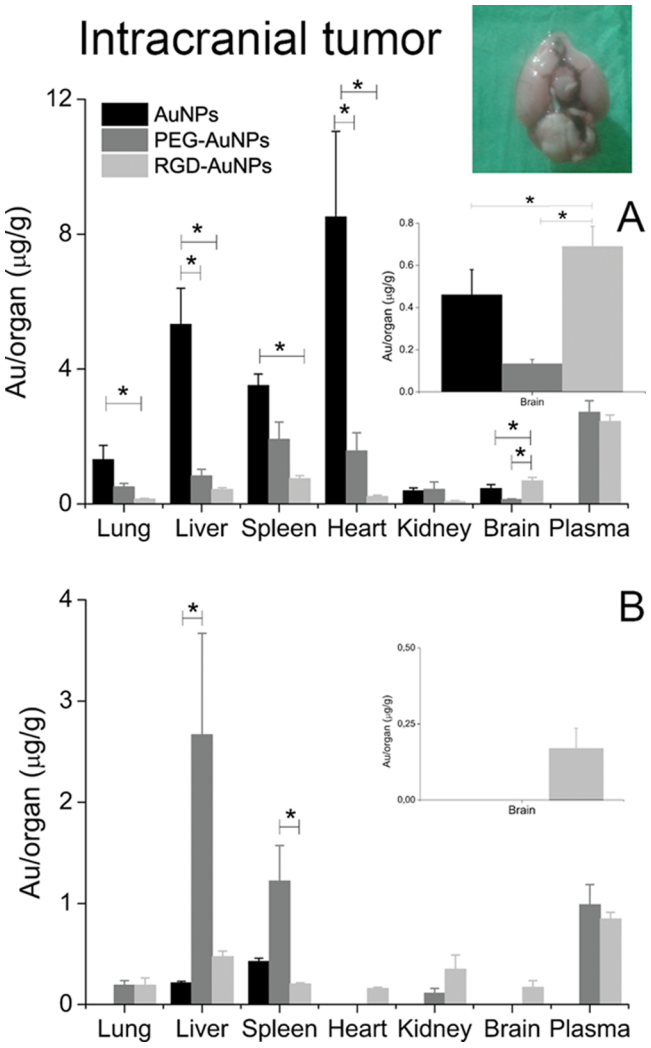

Figure 9. Quantitative biodistribution of intravenously injected NPs 2 h (A) and 8 h (B) after administration in mice grafted with the intracranial tumor. Data are expressed as mean ± SD; *p < 0.05 by Kruskal–Wallis test.

the highest affinity for $\alpha v\beta 3$ integrin, but they are able to bind the $\alpha v\beta 5$ and $\alpha 5\beta 1$ integrins as well, which can contribute to NP binding.[68,69]

The three different NP formulations probably take advantage of different pathways to gain access to the cytoplasmic component. As it is known that protein adsorption on the NP surface can mediate the uptake, it is reasonable to think that AuNPs exploit receptor-mediated endocytosis probably mediated by an albumin corona formed immediately after contact with the cell culture medium.[70,71] It is more difficult to speculate on the internalization mechanism of PEGylated NPs (PEG-AuNPs) as the literature reports of conflicting data and conclusions in this regard. Perhaps, the most convincing proposal is for a mechanism of endocytosis that is dependent on the size of the NPs.[72] On the contrary, it is reasonable to assume that RGD-AuNPs are principally internalized via an energy-dependent process through receptor-mediated endocytosis; this mechanism is confirmed by the results of our competition assay, in which pretreatment with the $\alpha v\beta 3$ integrin antibody reduced the uptake by about 60% (Figure 5B).[73] However, since the internalization was not completely inhibited, additional pathways and/or the binding with other integrins ($\alpha v\beta 5$ and $\alpha 5\beta 1$) probably contribute to the uptake of RGD-AuNPs.

The inhibition of network formation at a lower concentration can be reliably ascribed to the ability of GRGDG-NH_2 to bind and block the $\alpha v\beta 3$ integrin by acting as an integrin antagonist[74] blocking or decreasing cell migration and thus network formation.[75] Indeed, RGD-like peptides are able to block the integrin binding site by competing with the RGD-containing ligands (vibronectin, fibronectin).[76] Network destruction by RGD-AuNPs and GRGDG-NH_2 could be due to the ability of small RGD-like peptides to act as potent integrin antagonist compounds that can disrupt the $\alpha v\beta 3$ integrin–ligand interactions.[77]

Overall, the results obtained in the in vitro experiments can be explained by considering (i) the overexpression of $\alpha v\beta 3$ integrin in the B16F10 cell line, (ii) the affinity of RGD-like peptides for $\alpha v\beta 3$ integrin, and (iii) the critical role of this integrin isoform in cell migration and tumor growth.

In vivo biodistribution data have confirmed the ability of RGD-AuNPs to accumulate at the tumor site. However, differences in the biodistribution trend were observed.

When injected in animals with subcutaneous tumors, RGD-AuNPs showed high accumulation in the lungs and brain (Figure 8A). It may be speculated that part of this accumulation was due to the presence of brain and lung metastases. In fact, B16F10 cells have been used to create lung metastasis animal models (macroscopic metastasis with a volume between 6 and 400 mm^3) that generally develop 10–

DOI: 10.1021/acs.molpharmaceut.9b00047
Mol. Pharmaceutics 2019, 16, 2430–2444

15 days after the implant.[78] In the case of the subcutaneous graft, the time for macroscopic metastasis development is generally longer than 10−15 days.[79,80] For instance, 24 days after tumor cell inoculation (tumor diameter of 15 mm), 165 metastatic nodules were found in the lungs.[81]

In our experimental setup, macroscopic metastases were not observed during organ collection, but the presence of micrometastases cannot be excluded. In fact, it has been demonstrated that iodobenzamides, the compounds used for melanoma detection, accumulate in the lung and brain of subcutaneous melanoma mouse models.[82] For these reasons, it is possible that RGD-AuNPs were able to accumulate in the lungs and brain because of the presence of micrometastases in these organs. In addition, the inflammatory event associated with tumor and possibly micrometastases would have recruited infiltrating cells, such as neutrophils.[83,84] Since $\alpha v\beta 3$ integrins are expressed on monocytes and neutrophils and leucocytes are able to cross the BBB,[85] it may be that RGD-AuNPs were transported into the brain as a consequence of the inflammation.[86−88]

The biodistribution data obtained from the intracranial tumor models confirmed the hypothesis that RGD-AuNPs brain accumulation is due to receptor-mediated endocytosis by exploiting $\alpha v\beta 3$ integrin receptors on the BBB. In addition to the BBB crossing, another obstacle in the brain tumor therapy is the "blood−brain tumor barrier" (BBTB) due to the angiogenic processes associated with the tumor growth.[89] It is composed of three microvessel populations: continuous and nonfenestrated capillaries, continuous and fenestrated capillaries, and leaky capillaries.[90] The anatomy of this barrier depends mainly on the grade of the brain tumor.[91] In a low grade of glioma, the BBTB is predominantly composed of continuous and nonfenestrated capillaries, whereas in a high grade of glioma, it is mainly characterized by the presence of a leaky vasculature.[91] According to the mosaic vessel theory, the blood vessels surrounding the tumor are usually composed of normal endothelial cells and tumor cells,[7] and integrins are highly expressed on the BBTB.[92] Considering the peculiar anatomical characteristics of the BBTB, one way to overcome it could be receptor-mediated transcytosis, for which RGD-AuNPs may be particularly suited. Another factor that may explain RGD-AuNP accumulation in the brain is the $\alpha v\beta 3$ integrin overexpression in the tumor site itself; as demonstrated by the in vitro study, the B16F10 cell line is characterized by the overexpression of this receptor.

Finally, it is interesting to note the peculiar behavior of AuNPs: (i) the brain accumulation was lower than RGD-AuNPs but much higher than PEG-AuNPs and (ii) the organ with the highest gold accumulation was the heart (Figure 9A).

It may be speculated that both behaviors are explained by protein adsorption on the AuNP surface. In fact, the rapid disappearance of AuNPs from the plasma and their accumulation in the liver, spleen, and lungs is surely due to the opsonization process. However, some of the adsorbed proteins may act as a targeting moiety, allowing the targeting of different organs. Brain accumulation could be due to the adsorption of apolipoproteins E and A1 on particle surfaces[93] enabling the adhesion and/or crossing of the BBB.[94−96]

AuNPs heart accumulation has been previously reported by Schleh et al., demonstrating that the 18 nm AuNP has a higher trophism for the heart than AuNPs of other sizes.[97] In addition, NPs characterized by a charged surface and by a ζ-potential of about |30| mV can reach and accumulate in the heart.[98] However, the fact that the same accumulation was not seen in the animal bearing subcutaneous tumors makes reliable the hypothesis of a different protein corona surrounding the particles. In fact, bare NPs are generally distributed in the body as a function of the type and relative abundance of the proteins (as well as other biomolecules) adsorbed on their surfaces. Recent studies evidenced significant differences in the circulating proteins (and then in the protein corona formed around circulating NPs) of healthy and diseased animals[99] or in patients with different tumors.[100,101]

CONCLUSIONS

$\alpha v\beta 3$ integrin expression is prominent in different types of cancer, such as melanoma and glioblastoma, and in vessels formed during cancer development but not in normal vessels. Integrins regulate the angiogenic process, playing a critical role in tumor growth and invasion. For these reasons, they are an extremely interesting biological target for cancer diagnosis and therapy. RGD-AuNPs are able to bind this receptor with good affinity and to be internalized in cells characterized by integrin overexpression. All in vitro tests confirm that this formulation is more potent and more internalized in cells than AuNPs and PEG-AuNPs, supporting the idea that the presence of the GRGDG-NH_2 pentapeptide on the particle surface is the reason for its efficient particle uptake. Biodistribution studies highlighted the ability of RGD-AuNPs to accumulate in the brain and in subcutaneous tumors, possibly through active targeting. It is important to highlight that bare AuNPs showed biodistribution differences in the two tumor models. This could be due to a different protein corona formed in vivo. The capability of decorated AuNPs to reach tumor sites can be attributed to three synergic mechanisms: first, overexpression of $\alpha v\beta 3$ integrin in tumor cells; second, angiogenesis and integrin overexpression in tumor vessels and not in vessels of the healthy tissue; and third, the inflammation process and leucocyte recruitment. In conclusion, while ours is a preliminary study and more in-depth characterization should be performed, we have demonstrated the high potential of this carrier for diagnostic and therapeutic applications.

ASSOCIATED CONTENT

Supporting Information

The Supporting Information is available free of charge on the ACS Publications website at DOI: 10.1021/acs.molpharmaceut.9b00047.

Peptide design and optimization, methods and software, conformational searches of GRGDS and GRGDG-NH_2, docking studies of GRGDS and GRGDG-NH_2, $\Delta G_{binding}$ estimation, prediction of conformer populations, MD simulations of GRGDG-NH_2, peptide synthesis, experimental section, synthesis of **1a**, **2a**, **3a**, and **4a**, Fmoc-Asp(O*t*Bu)-Gly-NH_2 synthetic strategy optimization, NP preparation and characterization, MatLab script employed for particle size determination, NP PEGylation and decoration, stability evaluation of NPs employed in in vitro and in vivo studies, and data on cell viability used to calculate IC50 (PDF)

AUTHOR INFORMATION

Corresponding Author

*E-mail: paolo.blasi@unicam.it. Phone: +390737402726.

DOI: 10.1021/acs.molpharmaceut.9b00047
Mol. Pharmaceutics 2019, 16, 2430−2444

ORCID

Nunzio Iraci: 0000-0002-1359-8684
Anna Donnadio: 0000-0003-2903-4135
Andrea Temperini: 0000-0001-8702-2082
Paolo Blasi: 0000-0002-8543-4275

Notes

The authors declare no competing financial interest.

■ ACKNOWLEDGMENTS

This work was partially supported by the Fondazione Cassa di Risparmio di Perugia, project code: 2012.0248.021 RICERCA SCIENTIFICA E TECNOLOGICA. The author from the University of Salerno acknowledges Regione Campania for the financial support given by the grant PON-FESR 2014−2020 "Combattere la resistenza tumorale: piattaforma integrata multidisciplinare per un approccio tecnologico innovativo alle oncoterapie—Campania Oncoterapie" (Project N. B61G18000470007). The authors would like to thank Sheila Beatty for editing the the manuscript.

■ REFERENCES

(1) WHO. Cancer. http://www.who.int/cancer/en/ (accessed April 27, 2018).
(2) Marcucci, F.; Corti, A. How to Improve Exposure of Tumor Cells to Drugs: Promoter Drugs Increase Tumor Uptake and Penetration of Effector Drugs. *Adv. Drug Delivery Rev.* **2012**, *64*, 53−68.
(3) Burgess, D. J. Unravelling metabolic dependencies. *Nat. Rev. Cancer* **2012**, *12*, 321.
(4) Widakowich, C.; de Castro, G.; de Azambuja, E.; Dinh, P.; Awada, A. Review: Side Effects of Approved Molecular Targeted Therapies in Solid Cancers. *Oncologist* **2007**, *12*, 1443−1455.
(5) Pardridge, W. M. Drug Transport across the Blood-Brain Barrier. *J. Cereb. Blood Flow Metab.* **2012**, *32*, 1959−1972.
(6) Steichen, S. D.; Caldorera-Moore, M.; Peppas, N. A. A Review of Current Nanoparticle and Targeting Moieties for the Delivery of Cancer Therapeutics. *Eur. J. Pharm. Sci.* **2013**, *48*, 416−427.
(7) Folkman, J. Can Mosaic Tumor Vessels Facilitate Molecular Diagnosis of Cancer? *Proc. Natl. Acad. Sci. U.S.A.* **2001**, *98*, 398−400.
(8) Goodman, S. L.; Picard, M. Integrins as Therapeutic Targets. *Trends Pharmacol. Sci.* **2012**, *33*, 405−412.
(9) Desgrosellier, J. S.; Cheresh, D. A. Integrins in Cancer: Biological Implications and Therapeutic Opportunities. *Nat. Rev. Cancer* **2010**, *10*, 9−22.
(10) Hodivala-Dilke, K. $\alpha v\beta 3$ integrin and angiogenesis: a moody integrin in a changing environment. *Curr. Opin. Cell Biol.* **2008**, *20*, 514−519.
(11) Xiong, J.-P.; Stehle, T.; Zhang, R.; Joachimiak, A.; Frech, M.; Goodman, S. L.; Arnaout, M. A. Crystal Structure of the Extracellular Segment of Integrin alpha Vbeta 3 in Complex with an Arg-Gly-Asp Ligand. *Science* **2002**, *296*, 151−155.
(12) Chen, K.; Chen, X. Integrin Targeted Delivery of Chemotherapeutics. *Theranostics* **2011**, *1*, 189−200.
(13) Kim, J.-W.; Lee, H.-S. Tumor Targeting by Doxorubicin-RGD-4C Peptide Conjugate in an Orthotopic Mouse Hepatoma Model. *Int. J. Mol. Med.* **2004**, *14*, 529−535.
(14) Temperini, A.; Piazzolla, F.; Minuti, L.; Curini, M.; Siciliano, C. General, Mild, and Metal-Free Synthesis of Phenyl Selenoesters from Anhydrides and Their Use in Peptide Synthesis. *J. Org. Chem.* **2017**, *82*, 4588−4603.
(15) Schneider, C. A. NIH Image to ImageJ: 25 Years of Image Analysis. *Nat. Methods* **2012**, *9*, 671.
(16) MathWorks—Makers of MATLAB and Simulink. https://it.mathworks.com/ (accessed March 27, 2018).
(17) Ellman, G. L. Tissue Sulfhydryl Groups. *Arch. Biochem. Biophys.* **1959**, *82*, 70−77.
(18) Winther, J. R.; Thorpe, C. Quantification of Thiols and Disulfides. *Biochim. Biophys. Acta* **2014**, *1840*, 838−846.
(19) Bachelet, M.; Chen, R. Self-Assembly of PEGylated Gold Nanoparticles with Satellite Structures as Seeds. *Chem. Commun.* **2016**, *52*, 9542−9545.
(20) Riener, C. K.; Kada, G.; Gruber, H. J. Quick measurement of protein sulfhydryls with Ellman's reagent and with 4,4′-dithiodipyridine. *Anal. Bioanal. Chem.* **2002**, *373*, 266−276.
(21) Manson, J.; Kumar, D.; Meenan, B. J.; Dixon, D. Polyethylene Glycol Functionalized Gold Nanoparticles: The Influence of Capping Density on Stability in Various Media. *Gold Bull.* **2011**, *44*, 99−105.
(22) Elzey, S.; Tsai, D.-H.; Rabb, S. A.; Yu, L. L.; Winchester, M. R.; Hackley, V. A. Quantification of Ligand Packing Density on Gold Nanoparticles Using ICP-OES. *Anal. Bioanal. Chem.* **2012**, *403*, 145−149.
(23) Rabanel, J.-M.; Hildgen, P.; Banquy, X. Assessment of PEG on Polymeric Particles Surface, a Key Step in Drug Carrier Translation. *J. Controlled Release* **2014**, *185*, 71−87.
(24) Perry, J. L.; Reuter, K. G.; Kai, M. P.; Herlihy, K. P.; Jones, S. W.; Luft, J. C.; Napier, M.; Bear, J. E.; DeSimone, J. M. PEGylated PRINT Nanoparticles: The Impact of PEG Density on Protein Binding, Macrophage Association, Biodistribution, and Pharmacokinetics. *Nano Lett.* **2012**, *12*, 5304−5310.
(25) Roberts, M. J.; Bentley, M. D.; Harris, J. M. Chemistry for Peptide and Protein PEGylation. *Adv. Drug Delivery Rev.* **2002**, *54*, 459−476.
(26) Veronese, F. M. Peptide and protein PEGylation. *Biomaterials* **2001**, *22*, 405−417.
(27) Isidro-Llobet, A.; Albericio, F. Amino Acid-Protecting Groups. *Chem. Rev.* **2009**, *109*, 2455.
(28) Mondal, G.; Barui, S.; Chaudhuri, A. The relationship between the cyclic-RGDfK ligand and $\alpha v\beta 3$ integrin receptor. *Biomaterials* **2013**, *34*, 6249−6260.
(29) Vijayakumar, S.; Ganesan, S. In VitroCytotoxicity Assay on Gold Nanoparticles with Different Stabilizing Agents. *J. Nanomater.* **2012**, *2012*, 734398.
(30) Danhier, F.; Vroman, B.; Lecouturier, N.; Crokart, N.; Pourcelle, V.; Freichels, H.; Jérôme, C.; Marchand-Brynaert, J.; Feron, O.; Préat, V. Targeting of Tumor Endothelium by RGD-Grafted PLGA-Nanoparticles Loaded with Paclitaxel. *J. Controlled Release* **2009**, *140*, 166−173.
(31) Glauert, A. M.; Glauert, R. H. Araldite as an Embedding Medium for Electron Microscopy. *J. Cell Biol.* **1958**, *4*, 191−194.
(32) Engbring, J. A.; Hoffman, M. P.; Karmand, A. J.; Kleinman, H. K. The B16F10 Cell Receptor for a Metastasis-Promoting Site on Laminin-1 Is a Heparan Sulfate/Chondroitin Sulfate-Containing Proteoglycan. *Cancer Res.* **2002**, *62*, 3549−3554.
(33) Seymour, L. W.; Ulbrich, K.; Steyger, P.; Brereton, M.; Subr, V.; Strohalm, J.; Duncan, R. Tumour Tropism and Anti-Cancer Efficacy of Polymer-Based Doxorubicin Prodrugs in the Treatment of Subcutaneous Murine B16F10 Melanoma. *Br. J. Cancer* **1994**, *70*, 636−641.
(34) De Jong, W. H.; Hagens, W. I.; Krystek, P.; Burger, M. C.; Sips, A. J. A. M.; Geertsma, R. E. Particle Size-Dependent Organ Distribution of Gold Nanoparticles after Intravenous Administration. *Biomaterials* **2008**, *29*, 1912−1919.
(35) Xiong, J.-P.; Stehle, T.; Zhang, R.; Joachimiak, A.; Frech, M.; Goodman, S. L.; Arnaout, M. A. Crystal Structure of the Extracellular Segment of Integrin alpha Vbeta 3 in Complex with an Arg-Gly-Asp Ligand. *Science* **2002**, *296*, 151−155.
(36) Monferran, S.; Skuli, N.; Delmas, C.; Favre, G.; Bonnet, J.; Cohen-Jonathan-Moyal, E.; Toulas, C. $\alpha v\beta 3$ and $\alpha v\beta 5$ integrins control glioma cell response to ionising radiation through ILK and RhoB. *Int. J. Cancer* **2008**, *123*, 357−364.
(37) Eliceiri, B. P.; Cheresh, D. A. The Role of αv Integrins during Angiogenesis. *Mol. Med.* **1998**, *4*, 741−750.
(38) Desgrosellier, J. S.; Cheresh, D. A. Integrins in Cancer: Biological Implications and Therapeutic Opportunities. *Nat. Rev. Cancer* **2010**, *10*, 9−22.

DOI: 10.1021/acs.molpharmaceut.9b00047
Mol. Pharmaceutics 2019, 16, 2430−2444

(39) Seguin, L.; Desgrosellier, J. S.; Weis, S. M.; Cheresh, D. A. Integrins and Cancer: Regulators of Cancer Stemness, Metastasis, and Drug Resistance. *Trends Cell Biol.* **2015**, *25*, 234−240.
(40) Danhier, F.; Vroman, B.; Lecouturier, N.; Crokart, N.; Pourcelle, V.; Freichels, H.; Jérôme, C.; Marchand-Brynaert, J.; Feron, O.; Préat, V. Targeting of Tumor Endothelium by RGD-Grafted PLGA-Nanoparticles Loaded with Paclitaxel. *J. Controlled Release* **2009**, *140*, 166−173.
(41) Hackley, V. A.; Clogston, D. J. Measuring the Hydrodynamic Size of Nanoparticles in Aqueous Media Using Batch-Mode Dynamic Light Scattering. In *Characterization of Nanoparticles Intended for Drug Delivery*; McNeil, S. E., Ed.; Methods in Molecular Biology; Humana Press, 2011; pp 35−52.
(42) Theory and Application of Morphological Analysis: Fine Particles and Surfaces. https://www.crcpress.com/Theory-and-Application-of-Morphological-Analysis-Fine-Particles-and-Surfaces/Luerkens/p/book/9780849367779 (accessed March 27, 2018).
(43) Li, Y.; Kröger, M.; Liu, W. K. Endocytosis of PEGylated Nanoparticles Accompanied by Structural and Free Energy Changes of the Grafted Polyethylene Glycol. *Biomaterials* **2014**, *35*, 8467−8478.
(44) Ramos, O. H. P.; Kauskot, A.; Cominetti, M. R.; Bechyne, I.; Salla Pontes, C. L.; Chareyre, F.; Manent, J.; Vassy, R.; Giovannini, M.; Legrand, C.; et al. A novel $\alpha v\beta 3$-blocking disintegrin containing the RGD motive, DisBa-01, inhibits bFGF-induced angiogenesis and melanoma metastasis. *Clin. Exp. Metastasis* **2008**, *25*, 53−64.
(45) Monferran, S.; Skuli, N.; Delmas, C.; Favre, G.; Bonnet, J.; Cohen-Jonathan-Moyal, E.; Toulas, C. $\alpha v\beta 3$ and $\alpha v\beta 5$ integrins control glioma cell response to ionising radiation through ILK and RhoB. *Int. J. Cancer* **2008**, *123*, 357−364.
(46) Sieuwerts, A. M.; Klijn, J. G.; Peters, H. A.; Foekens, J. A. The MTT Tetrazolium Salt Assay Scrutinized: How to Use This Assay Reliably to Measure Metabolic Activity of Cell Cultures in Vitro for the Assessment of Growth Characteristics, IC50-Values and Cell Survival. *Clin. Chem. Lab. Med.* **1995**, *33*, 813−823.
(47) Capek, I. On Biodecorated Gold Nanoparticles Distributed within Tissues and Cells. *J. Nanomed. Res.* **2015**, *2*, 1−10.
(48) Kramer, R. H.; Bensch, K. G.; Wong, J. Invasion of Reconstituted Basement Membrane Matrix by Metastatic Human Tumor Cells. *Cancer Res.* **1986**, *46*, 1980−1989.
(49) Aboody, K. S.; Najbauer, J.; Schmidt, N. O.; Yang, W.; Wu, J. K.; Zhuge, Y.; Przylecki, W.; Carroll, R.; Black, P. M.; Perides, G. Targeting of Melanoma Brain Metastases Using Engineered Neural Stem/Progenitor Cells. *Neurooncology* **2006**, *8*, 119−126.
(50) Torchilin, V. P. Passive and Active Drug Targeting: Drug Delivery to Tumors as an Example. *Handb. Exp. Pharmacol.* **2010**, *197*, 3−53.
(51) Maeda, H.; Wu, J.; Sawa, T.; Matsumura, Y.; Hori, K. Tumor Vascular Permeability and the EPR Effect in Macromolecular Therapeutics: A Review. *J. Controlled Release* **2000**, *65*, 271−284.
(52) Torchilin, V. Tumor Delivery of Macromolecular Drugs Based on the EPR Effect. *Adv. Drug Delivery Rev.* **2011**, *63*, 131−135.
(53) Montet, X.; Montet-Abou, K.; Reynolds, F.; Weissleder, R.; Josephson, L. Nanoparticle Imaging of Integrins on Tumor Cells. *Neoplasia* **2006**, *8*, 214−222.
(54) Taga, T.; Suzuki, A.; Gonzalez-Gomez, I.; Gilles, F. H.; Stins, M.; Shimada, H.; Barsky, L.; Weinberg, K. I.; Laug, W. E. Alpha V-Integrin Antagonist EMD 121974 Induces Apoptosis in Brain Tumor Cells Growing on Vitronectin and Tenascin. *Int. J. Cancer* **2002**, *98*, 690−697.
(55) Mathieu, V.; Mijatovic, T.; van Damme, M.; Kiss, R. Gastrin Exerts Pleiotropic Effects on Human Melanoma Cell Biology. *Neoplasia* **2005**, *7*, 930−943.
(56) Eliceiri, B. P.; Cheresh, D. A. The Role of αv Integrins during Angiogenesis. *Mol. Med.* **1998**, *4*, 741−750.
(57) Varner, J. A.; Cheresh, D. A. Tumor Angiogenesis and the Role of Vascular Cell Integrin Alphavbeta3. In *Important Advances in Oncology*; DeVita, V. T., Hellman, S., Rosenberg, S. A., Eds.; Lippincott, Williams & Wilkins, 1996; pp 69−87.
(58) Rüegg, C.; Yilmaz, A.; Bieler, G.; Bamat, J.; Chaubert, P.; Lejeune, F. J. Evidence for the involvement of endotheliai cell integrin $\alpha V\beta 3$ in the disruption of the tumor vascuiature induced by TNF and IFN-γ. *Nat. Med.* **1998**, *4*, 408−414.
(59) Lin, R.-Y.; Dayananda, K.; Chen, T.-J.; Chen, C.-Y.; Liu, G.-C.; Lin, K.-L.; Wang, Y.-M. Targeted RGD Nanoparticles for Highly Sensitive in Vivo Integrin Receptor Imaging. *Contrast Media Mol. Imaging* **2012**, *7*, 7−18.
(60) Silginer, M.; Weller, M.; Ziegler, U.; Roth, P. Integrin Inhibition Promotes Atypical Anoikis in Glioma Cells. *Cell Death Dis.* **2014**, *5*, No. e1012.
(61) Alcantar, N. A.; Aydil, E. S.; Israelachvili, J. N. Polyethylene Glycol-Coated Biocompatible Surfaces. *J. Biomed. Mater. Res.* **2000**, *51*, 343−351.
(62) Verma, A.; Stellacci, F. Effect of Surface Properties on Nanoparticle Cell Interactions. *Small* **2010**, *6*, 12−21.
(63) Tsai, D.-H.; DelRio, F. W.; Keene, A. M.; Tyner, K. M.; MacCuspie, R. I.; Cho, T. J.; Zachariah, M. R.; Hackley, V. A. Adsorption and Conformation of Serum Albumin Protein on Gold Nanoparticles Investigated Using Dimensional Measurements and in Situ Spectroscopic Methods. *Langmuir* **2011**, *27*, 2464−2477.
(64) Allouni, Z. E.; Gjerdet, N. R.; Cimpan, M. R.; Høl, P. J. The effect of blood protein adsorption on cellular uptake of anatase TiO2 nanoparticles. *Int. J. Nanomedicine* **2015**, *10*, 687−695.
(65) Andersen, L.; Dinesen, B.; Jørgensen, P. N.; Poulsen, F.; Røder, M. E. Enzyme Immunoassay for Intact Human Insulin in Serum or Plasma. *Clin. Chem.* **1993**, *39*, 578−582.
(66) Vogel, B. E.; Lee, S.-J.; Hildebrand, A.; Craig, W.; Pierschbacher, M. D.; Wong-Staal, F.; Ruoslahti, E. A Novel Integrin Specificity Exemplified by Binding of the Alpha v Beta 5 Integrin to the Basic Domain of the HIV Tat Protein and Vitronectin. *J. Cell Biol.* **1993**, *121*, 461−468.
(67) Mitjans, F.; Sander, D.; Adán, J.; Sutter, A.; Martinez, J. M.; Jäggle, C. S.; Moyano, J. M.; Kreysch, H. G.; Piulats, J.; Goodman, S. L. An Anti-Alpha v-Integrin Antibody That Blocks Integrin Function Inhibits the Development of a Human Melanoma in Nude Mice. *J. Cell Sci.* **1995**, *108*, 2825−2838.
(68) Koivunen, E.; Wang, B.; Ruoslahti, E. Phage Libraries Displaying Cyclic Peptides with Different Ring Sizes: Ligand Specificities of the RGD-Directed Integrins. *Nat. Biotechnol.* **1995**, *13*, 265−270.
(69) Wacker, B. K.; Alford, S. K.; Scott, E. A.; Das Thakur, M.; Longmore, G. D.; Elbert, D. L. Endothelial Cell Migration on RGD-Peptide-Containing PEG Hydrogels in the Presence of Sphingosine 1-Phosphate. *Biophys. J.* **2008**, *94*, 273−285.
(70) Alkilany, A. M.; Murphy, C. J. Toxicity and Cellular Uptake of Gold Nanoparticles: What We Have Learned so Far? *J. Nanopart. Res.* **2010**, *12*, 2313−2333.
(71) Conner, S. D.; Schmid, S. L. Regulated Portals of Entry into the Cell. *Nature* **2003**, *422*, 37−44.
(72) Chuang, K.-H.; Wang, H.-E.; Chen, F.-M.; Tzou, S.-C.; Cheng, C.-M.; Chang, Y.-C.; Tseng, W.-L.; Shiea, J.; Lin, S.-R.; Wang, J.-Y.; et al. Endocytosis of PEGylated Agents Enhances Cancer Imaging and Anticancer Efficacy. *Mol. Cancer Ther.* **2010**, *9*, 1903−1912.
(73) Yao, W.; Xu, P.; Zhao, J.; Ling, L.; Li, X.; Zhang, B.; Cheng, N.; Pang, Z. RGD Functionalized Polymeric Nanoparticles Targeting Periodontitis Epithelial Cells for the Enhanced Treatment of Periodontitis in Dogs. *J. Colloid Interface Sci.* **2015**, *458*, 14−21.
(74) Shimaoka, M.; Springer, T. A. Therapeutic Antagonists and Conformational Regulation of Integrin Function. *Nat. Rev. Drug Discovery* **2003**, *2*, 703−716.
(75) Georgoulis, A.; Havaki, S.; Drosos, Y.; Goutas, N.; Vlachodimitropoulos, D.; Aleporou-Marinou, V.; Kittas, C.; Marinos, E.; Kouloukoussa, M. RGD Binding to Integrin Alphavbeta3 Affects Cell Motility and Adhesion in Primary Human Breast Cancer Cultures. *Ultrastruct. Pathol.* **2012**, *36*, 387−399.
(76) Legler, D. F.; Wiedle, G.; Ross, F. P.; Imhof, B. A. Superactivation of Integrin Alphavbeta3 by Low Antagonist Concentrations. *J. Cell Sci.* **2001**, *114*, 1545−1553.

DOI: 10.1021/acs.molpharmaceut.9b00047
Mol. Pharmaceutics 2019, 16, 2430−2444

(77) Weis, S. M.; Cheresh, D. A. v Integrins in Angiogenesis and Cancer. *Cold Spring Harbor Perspect. Med.* **2011**, *1*, a006478.
(78) Winkelmann, C. T.; Figueroa, S. D.; Rold, T. L.; Volkert, W. A.; Hoffman, T. J. Microimaging Characterization of a B16-F10 Melanoma Metastasis Mouse Model. *Mol. Imaging* **2006**, *5*, 105−114.
(79) Nathanson, S. D.; Haas, G. P.; Mead, M. J.; Lee, M. Spontaneous regional lymph node metastases of three variants of the B16 melanoma: Relationship to primary tumor size and pulmonary metastas. *J. Surg. Oncol.* **1986**, *33*, 41−45.
(80) Eberting, C. L. D.; Shrayer, D. P.; Butmarc, J.; Falanga, V. Histologic Progression of B16 F10 Metastatic Melanoma in C57BL/6 Mice over a Six Week Time Period: Distant Metastases before Local Growth. *J. Dermatol.* **2004**, *31*, 299−304.
(81) Forde, P. F.; Sadadcharam, M.; Hall, L. J.; O'Donovan, T. R.; de Kruijf, M.; Byrne, W. L.; O'Sullivan, G. C.; Soden, D. M. Enhancement of Electroporation Facilitated Immunogene Therapy via T-Reg Depletion. *Cancer Gene Ther.* **2014**, *21*, 349−354.
(82) Cheng, Z.; Mahmood, A.; Li, H.; Davison, A.; Jones, A. G. [99mTcOAADT]-(CH2)2-Net2: A Potential Small-Molecule Single-Photon Emission Computed Tomography Probe for Imaging Metastatic Melanoma. *Cancer Res.* **2005**, *65*, 4979−4986.
(83) Carmona-Bayonas, A. Acute Inflammation and Micrometastasis Proliferation: A Fissure in the Uniformitarian Façade of Cancer. *Jpn. J. Clin. Oncol.* **2009**, *39*, 192−194.
(84) Wu, H.; Cabral, H.; Toh, K.; Mi, P.; Chen, Y.-C.; Matsumoto, Y.; Yamada, N.; Liu, X.; Kinoh, H.; Miura, Y.; et al. Polymeric Micelles Loaded with Platinum Anticancer Drugs Target Preangiogenic Micrometastatic Niches Associated with Inflammation. *J. Controlled Release* **2014**, *189*, 1−10.
(85) Miller, D. W. Immunobiology of the Blood-Brain Barrier. *J. NeuroVirol.* **1999**, *5*, 570−578.
(86) Zhan, C.; Gu, B.; Xie, C.; Li, J.; Liu, Y.; Lu, W. Cyclic RGD Conjugated Poly(Ethylene Glycol)-Co-Poly(Lactic Acid) Micelle Enhances Paclitaxel Anti-Glioblastoma Effect. *J. Controlled Release* **2010**, *143*, 136−142.
(87) Jain, S.; Mishra, V.; Singh, P.; Dubey, P. K.; Saraf, D. K.; Vyas, S. P. RGD-Anchored Magnetic Liposomes for Monocytes/Neutrophils-Mediated Brain Targeting. *Int. J. Pharm.* **2003**, *261*, 43−55.
(88) Qin, J.; Chen, D.; Hu, H.; Cui, Q.; Qiao, M.; Chen, B. Surface Modification of RGD-Liposomes for Selective Drug Delivery to Monocytes/Neutrophils in Brain. *Chem. Pharm. Bull.* **2007**, *55*, 1192−1197.
(89) Miura, Y.; Takenaka, T.; Toh, K.; Wu, S.; Nishihara, H.; Kano, M. R.; Ino, Y.; Nomoto, T.; Matsumoto, Y.; Koyama, H.; et al. Cyclic RGD-Linked Polymeric Micelles for Targeted Delivery of Platinum Anticancer Drugs to Glioblastoma through the Blood-Brain Tumor Barrier. *ACS Nano* **2013**, *7*, 8583−8592.
(90) Groothuis, D. R. The Blood-Brain and Blood-Tumor Barriers: A Review of Strategies for Increasing Drug Delivery. *Neurooncology* **2000**, *2*, 45−59.
(91) van Tellingen, O.; Yetkin-Arik, B.; de Gooijer, M. C.; Wesseling, P.; Wurdinger, T.; de Vries, H. E. Overcoming the Blood-Brain Tumor Barrier for Effective Glioblastoma Treatment. *Drug Resist. Updates* **2015**, *19*, 1−12.
(92) Wei, X.; Gao, J.; Zhan, C.; Xie, C.; Chai, Z.; Ran, D.; Ying, M.; Zheng, P.; Lu, W. Liposome-Based Glioma Targeted Drug Delivery Enabled by Stable Peptide Ligands. *J. Controlled Release* **2015**, *218*, 13−21.
(93) Schäffler, M.; Semmler-Behnke, M.; Sarioglu, H.; Takenaka, S.; Wenk, A.; Schleh, C.; Hauck, S. M.; Johnston, B. D.; Kreyling, W. G. Serum Protein Identification and Quantification of the Corona of 5, 15 and 80 Nm Gold Nanoparticles. *Nanotechnology* **2013**, *24*, 265103.
(94) Kreuter, J.; Hekmatara, T.; Dreis, S.; Vogel, T.; Gelperina, S.; Langer, K. Covalent Attachment of Apolipoprotein A-I and Apolipoprotein B-100 to Albumin Nanoparticles Enables Drug Transport into the Brain. *J. Controlled Release* **2007**, *118*, 54−58.
(95) Kreuter, J.; Shamenkov, D.; Petrov, V.; Ramge, P.; Cychutek, K.; Koch-Brandt, C.; Alyautdin, R. Apolipoprotein-Mediated Transport of Nanoparticle-Bound Drugs across the Blood-Brain Barrier. *J. Drug Targeting* **2002**, *10*, 317−325.
(96) Dal Magro, R.; Albertini, B.; Beretta, S.; Rigolio, R.; Donzelli, E.; Chiorazzi, A.; Ricci, M.; Blasi, P.; Sancini, G. Artificial Apolipoprotein Corona Enables Nanoparticle Brain Targeting. *Nanomedicine* **2018**, *14*, 429−438.
(97) Schleh, C.; Semmler-Behnke, M.; Lipka, J.; Wenk, A.; Hirn, S.; Schäffler, M.; Schmid, G.; Simon, U.; Kreyling, W. G. Size and Surface Charge of Gold Nanoparticles Determine Absorption across Intestinal Barriers and Accumulation in Secondary Target Organs after Oral Administration. *Nanotoxicology* **2012**, *6*, 36−46.
(98) Alexis, F.; Pridgen, E.; Molnar, L. K.; Farokhzad, O. C. Factors Affecting the Clearance and Biodistribution of Polymeric Nanoparticles. *Mol. Pharm.* **2008**, *5*, 505−515.
(99) Hadjidemetriou, M.; Al-Ahmady, Z.; Buggio, M.; Swift, J.; Kostarelos, K. A Novel Scavenging Tool for Cancer Biomarker Discovery Based on the Blood-Circulating Nanoparticle Protein Corona. *Biomaterials* **2019**, *188*, 118−129.
(100) Colapicchioni, V.; Tilio, M.; Digiacomo, L.; Gambini, V.; Palchetti, S.; Marchini, C.; Pozzi, D.; Occhipinti, S.; Amici, A.; Caracciolo, G. Personalized Liposome-Protein Corona in the Blood of Breast, Gastric and Pancreatic Cancer Patients. *Int. J. Biochem. Cell Biol.* **2016**, *75*, 180−187.
(101) Corbo, C.; Molinaro, R.; Tabatabaei, M.; Farokhzad, O. C.; Mahmoudi, M. Personalized Protein Corona on Nanoparticles and Its Clinical Implications. *Biomater. Sci.* **2017**, *5*, 378−387.

DOI: 10.1021/acs.molpharmaceut.9b00047
Mol. Pharmaceutics 2019, 16, 2430−2444